

# A thermodynamic nonequilibrium model for preferential infiltration and refreezing of melt in snow

Adrian Moure<sup>1</sup>, Nathan Jones<sup>1</sup>, Joshua Pawlak<sup>1</sup>, Colin Meyer<sup>2</sup>, Xiaojing Fu<sup>1</sup>

<sup>1</sup>Department of Mechanical and Civil Engineering, California Institute of Technology, Pasadena, CA,  
United States

<sup>2</sup>Thayer School of Engineering, Dartmouth College, Hanover, NH, United States

## Key Points:

- We propose a continuum model of gravity-driven preferential flow and refreezing of meltwater through porous snow;
- Compared to stable infiltration, channelized flow prolongs the travel path of melt and deepens its thermal impact on snow;
- We predict partially refrozen melt channels form vertical low porosity annulus consistent with ice pipes seen in field observations.

---

Corresponding author: Adrian Moure, [amoure@caltech.edu](mailto:amoure@caltech.edu)

Corresponding author: Xiaojing Fu, [rubyfu@caltech.edu](mailto:rubyfu@caltech.edu)

## Abstract

The transport of meltwater through porous snow is a fundamental process in hydrology that remains poorly understood but essential for more robust prediction of how the cryosphere will respond under climate change. Here we propose a continuum model that resolves the nonlinear coupling of preferential melt flow and the nonequilibrium thermodynamics of ice-melt phase change at the Darcy scale. We assume that the commonly observed unstable melt infiltration is due to the gravity fingering instability, and capture it using the modified Richards equation that is extended with a higher-order term in saturation. Our model accounts for changes in porosity and the thermal budget of the snowpack caused by melt refreezing at the continuum scale, based on a mechanistic estimate of the ice-water phase change kinetics formulated at the pore scale. We validate the model in 1D against field data and laboratory experiments of infiltration in snow and find generally good agreement. Compared to existing theory of stable melt infiltration, our 2D simulation results show that preferential infiltration delivers melt faster to deeper depths, and as a result, changes in porosity and temperature can occur at deeper parts of the snow. The simulations also capture the formation of vertical low porosity annulus known as ice pipes, which have been observed in the field but lack mechanistic understanding to date. Our results demonstrate how melt refreezing and unstable infiltration reshape the porosity structure of snow and impacts thermal and mass transport in highly nonlinear ways, which are not captured by simpler models.

## 1 Introduction

Water stored in snow and ice counts for 75% of Earth’s freshwater volume. Reliable predictions of the hydrological cycle in cold environments such as terrestrial snowpack and glaciers remain challenging, but are necessary to improve both water resources and geohazards management under climate variability. A fundamental process that remains poorly understood is how surface-generated melt—water released from its frozen state due to heating of the snow—transports and distributes within the snowpack before entering the groundwater or surface water systems. A robust model for meltwater flow through snow is crucial to formulate reliable predictions in larger-scale models of snow cryohydrology and glaciology.

One key challenge of modeling snowmelt hydrology is the ability to robustly capture the infiltration rate and storage location of meltwater within the snowpack. While

the generation of melt at snow surface can be relatively uniform in space, meltwater infiltration through the underlying snowpack is known to be highly heterogeneous in nature, forming (1) vertical preferential flow pathways that channelize meltwater (e.g., ice pipes) and (2) lateral flow pathways guided by horizontal low permeability zones (e.g., capillary barriers or ice lenses). Both types of preferential pathways have been observed in the field directly or indirectly (Campbell et al., 2006; Humphrey et al., 2012; Kinar & Pomeroy, 2015; Culberg et al., 2021; Clerx et al., 2022), but systematic investigation and mechanistic understanding of these phenomena are lacking. In particular, laboratory experiments in 3D samples (Waldner et al., 2004; Katsushima et al., 2013; Avanzi et al., 2016) have shown the percolation of meltwater into 3D snowpack/column to be intrinsically unstable, analogous to gravity-driven water infiltration through dry soil (Glass et al., 1989; Selker et al., 1992; Glass & Nicholl, 1996). However, direct observation of this process is difficult due to the opacity of snow. Additionally, when melt interacts with subfreezing snowpack, it can readily refreeze as ice and decrease local snow porosity. This refreezing process reduces the effective infiltration rate by both consuming liquid water available for transport and by lowering the hydraulic conductivity of snow, which hinders vertical percolation and promotes lateral runoff (Culberg et al., 2021; Clerx et al., 2022). The resulting heterogeneous porosity structures, such as ice pipes or ice lenses, play an important role in snow hydrology and geohazard assessment but the mechanism of their formation remains poorly understood.

Existing models of snowmelt transport are limited by simplified flow physics and thermodynamics and fail to address the important phenomena observed in the field as mentioned above. Meltwater infiltration through snowpack is traditionally modeled using the Richards equation (S. Colbeck, 1972; S. C. Colbeck, 1976). However, the Richards equation does not readily reproduce unstable infiltration patterns in 2D and is therefore limited in its ability to capture nonlinearity in drainage dynamics (DiCarlo, 2010, 2013). Within the snow hydrology literature, more recent models have explored alternatives or extensions to the Richards equation in order to capture unstable infiltration of meltwater (Hirashima et al., 2014, 2019; Leroux & Pomeroy, 2019; Leroux et al., 2020). These studies assume the snowpack is at the melting point (isothermal condition) such that no phase change occurs between melt and ice. Although this neglects an important aspect of the physics involved, these isothermal models have proved useful in providing insight into unstable melt infiltration. In these models, the Richards equation and the van Genuchten

model for capillary pressure (Van Genuchten, 1980) have been adapted for snow hydrology by empirically calibrating the water retention curve via infiltration experiments (Yamaguchi et al., 2010, 2012). Some authors have improved the capabilities of these models by accounting for imbibition and draining hysteresis (Leroux & Pomeroy, 2017) or a dynamic capillary pressure (Leroux & Pomeroy, 2019). However, an initial random distribution for the snow density and/or grain size is required to produce the phenomenon of preferential flow in these models (Hirashima et al., 2014; Leroux & Pomeroy, 2019).

In order to capture melting and freezing processes, isothermal models from the 1970s (S. Colbeck, 1972) have since been expanded to consider non-isothermal effects from the release of latent heat during melt-ice phase change and its impact on the thermal energy balance of the snowpack (Illangasekare et al., 1990). Most non-isothermal models of meltwater infiltration have considered a single temperature field to account for both the melt and ice phase (Illangasekare et al., 1990; Leroux & Pomeroy, 2017; Meyer & Hewitt, 2017), which implies that ice in contact with liquid water reaches the melting point instantaneously (always at equilibrium) and thus meltwater is always at the melting point. Limited by this equilibrium assumption, the rate of phase change needs to be prescribed (Leroux & Pomeroy, 2017) or based on empirical functions of temperature (Illangasekare et al., 1990; De Michele et al., 2013), which do not resolve the nonequilibrium thermodynamics during melt refreezing and can over- or under-estimate the refreezing rate. Some authors have reformulated the non-isothermal problem in terms of two unknowns: the enthalpy and the total water content (Aschwanden et al., 2012; Meyer & Hewitt, 2017). This type of model also considers thermal equilibrium, which allows for estimation of the liquid water saturation, porosity, and snow temperature from the enthalpy and total water content, enabling a simpler problem formulation. Some of these models (Illangasekare et al., 1990; De Michele et al., 2013; Leroux & Pomeroy, 2017; Meyer & Hewitt, 2017) account for changes in porosity due to melting and refreezing; however, they mainly focus on 1D scenarios and do not investigate the formation of macroscopic porosity structures in 2D or 3D such as ice pipes or ice lenses.

Here, we propose a model that couples the physics of unstable water infiltration in unsaturated porous media with the nonequilibrium thermodynamics of ice-water phase transitions at the Darcy-scale using a continuum description. To capture unstable melt infiltration, we adopt the framework proposed by Cueto-Felgueroso & Juanes (2008, 2009b) that extends the Richards equation with a higher-order term of the saturation gradient.

Such extension has been shown to give rise to a gravity fingering instability and requires only a small number of model parameters. In comparison to other recent models of unstable meltwater infiltration (Hirashima et al., 2014; Leroux & Pomeroy, 2017; Leroux et al., 2020), the infiltration model we adopt has a simpler formulation while remaining still robust in producing infiltration patterns consistent with experimental observations (Cueto-Felgueroso & Juanes, 2009b; Cueto-Felgueroso et al., 2020a,b). The model accounts for the phase change process of melt refreezing to ice by (1) modeling a decrease in local snow porosity due to refreezing and (2) updating the thermal budget based on the release of latent heat. Contrary to previous meltwater infiltration models that consider thermal equilibrium, our model assumes local thermal non-equilibrium (LTNE), which permits that the ice and water phases may coexist at different temperatures. The LTNE assumption allows us to mechanistically estimate the rate of ice-water phase change as a function of both the ice and water temperatures. The LTNE model has been recently used to improve thermodynamic description of frozen soil (Hamidi et al., 2019; Heinze, 2021), and, to the best of our knowledge, has not been used to investigate the thermodynamics of snowpack. The thermodynamic component of this model can be readily used to investigate melting instead of refreezing.

To organize this paper, we first provide the complete description of the model (Section 2) and its numerical implementation in the FEM framework (Section 3). In Section 4, we first perform limited model validations using laboratory experiments and field observations. In particular, we compare 1D numerical results with recent experimental studies that measure the hydraulic properties of snow under isothermal conditions in Sections 4.1.1 and 4.1.2 and with the thermal profile observed in the field during melt infiltration and refreezing in Section 4.1.3. We then present 2D simulations of our model in its reduced form under isothermal conditions (Section 4.2), and then in its full form under non-isothermal conditions (Section 4.3), and show its ability to capture preferential melt flow coupled with melt refreezing that lead to the formation of heterogeneous porosity structures when melt infiltrates into subfreezing snow.

## 2 Mathematical model

We propose a Darcy-scale model for unstable meltwater infiltration and refreezing through a snowpack. Here, we consider a snowpack as a porous medium composed of ice, air, and liquid water (Fig. 1). For simplicity, we refer to liquid water as *water* from

here on. The model unknowns are defined here as averaged quantities over a representative elementary volume (REV) and are (Fig. 1, inset): porosity  $\phi(\mathbf{x}, t)$ , saturation  $S(\mathbf{x}, t)$ , Darcy velocity of meltwater flow  $\mathbf{u}(\mathbf{x}, t)$ , ice temperature  $T_i(\mathbf{x}, t)$ , and water temperature  $T_w(\mathbf{x}, t)$ . Here,  $\mathbf{x}$  denotes spatial coordinates and  $t$  denotes time. The liquid water content (LWC) is computed as  $LWC = \phi S$  and the relative volume of ice as  $1 - \phi$ . Our model accounts for the ice-water phase transitions, i.e., melting and freezing. We disregard phase transitions involving water vapor because their kinetics are much slower than the time scale we consider in this work (Kaempfer & Schneebeli, 2007). We describe the model equations in the following paragraphs.

## 2.1 Mass conservation

The ice mass conservation equation can be written as

$$\rho_i \frac{\partial(1 - \phi)}{\partial t} = -\rho_i R_m W_{\text{SSA}} (T_{\text{int}} - T_{\text{melt}}), \quad (1)$$

where  $\rho_i$  is the ice density, which we assume constant,  $R_m$  is the phase change rate coefficient,  $W_{\text{SSA}}$  is the wet specific surface area,  $T_{\text{int}}$  is the volume-averaged temperature of the ice-water interface, and  $T_{\text{melt}}$  is the melting point. The right-hand side in Eq. (1) accounts for the amount of ice mass lost/gained due to melting/refreezing, and results from upscaling the Wilson-Frenkel law (Libbrecht, 2017) for ice growth (see Appendix for more details). Note that we do not consider snow compaction here. The coefficient  $R_m$  is defined as  $R_m = c_{p,w} / (L_{\text{sol}} \beta_{\text{sol}})$ , where  $c_{p,w}$  is the specific heat capacity of water,  $L_{\text{sol}}$  is the solidification latent heat, and  $\beta_{\text{sol}}$  is the kinetic attachment coefficient for ice growth from liquid water (Libbrecht, 2017), which we assume is constant.

$W_{\text{SSA}}$  represents the water-ice interfacial area per unit volume (units  $\text{m}^2 \text{m}^{-3}$ ). We follow Koponen et al. (1997) and assume that the snow specific surface area (SSA) evolves as a function of porosity such that  $\text{SSA} \sim \phi \ln(\phi)$ . Note that Domine et al. (2007) and Matzl & Schneebeli (2006) reported similar trends of SSA for different types of snow. We also assume that the relative amount of ice surface in contact with water with respect to the total ice surface is proportional to  $S$ . Thus, we can express  $W_{\text{SSA}}$  as

$$W_{\text{SSA}}(\phi, S) = S \frac{\text{SSA}_0}{\phi_0 \ln(\phi_0)} \phi \ln(\phi), \quad (2)$$

where  $\text{SSA}_0$  is the initial SSA of a snowpack with porosity  $\phi_0$ . The estimation of  $T_{\text{int}}$  is explained below in Section 2.2.1.

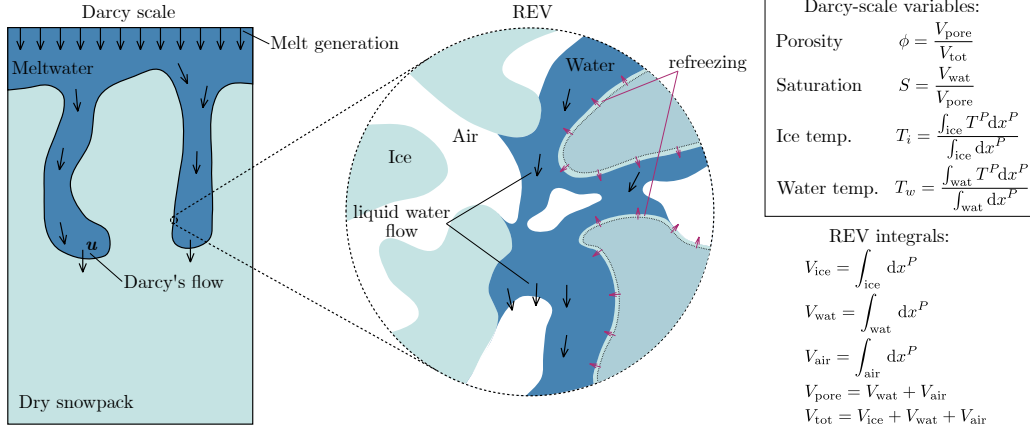


**Figure 1. Model description and unknowns.** Meltwater infiltration through the snowpack is modeled at the Darcy scale as an unsaturated flow within an evolving porous medium. Changes in the snow microstructure are caused by ice-liquid water phase changes. The problem unknowns (right inset), which are continuous at the Darcy scale, represent the volume averaged quantities in a Representative Elementary Volume (REV). The superscript  $P$  in the right-hand side expressions denotes pore-scale variables.

The water mass conservation equation reads

$$\rho_w \left( \frac{\partial(\phi S)}{\partial t} + \nabla \cdot \mathbf{u} \right) = \rho_i R_m W_{\text{SSA}} (T_{\text{int}} - T_{\text{melt}}), \quad (3)$$

where  $\rho_w$  is the water density, which we assume constant. Eq. (3) is an advection-reaction equation and accounts for the meltwater flow and the ice-water phase change. The right-hand side terms in Eq. (3) and in Eq. (1) have the same magnitude but opposite signs, which ensures mass conservation during ice-water phase transitions.

### 2.1.1 Unsaturated meltwater flow

The flow of meltwater through partially dry snow is often modeled using the Richards equation, which is the classic model for unsaturated gravity-driven flow through porous media. However, the Richards equation is known to reproduce only stable infiltration front and does not capture unstable infiltration phenomena known as gravity fingering, which has been observed during water infiltration through natural porous media such as sand, soil, and snow (DiCarlo, 2013; Humphrey et al., 2012; Avanzi et al., 2016).

Here, we use a natural extension of Richards equation proposed in Cueto-Felgueroso & Juanes (2008, 2009b) to model unstable meltwater infiltration. The meltwater velocity is expressed as

$$\mathbf{u} = -K_s(\phi)k_r(S)\nabla\Pi(S), \quad (4)$$

where  $K_s$  is the saturated hydraulic conductivity,  $k_r$  is the relative permeability, and  $\Pi$  is the total flow potential. We follow Calonne et al. (2012) and use the empirical expression for snow hydraulic conductivity

$$K_s(\phi) = 3 \left( \frac{d_i}{2} \right)^2 \frac{\rho_w g}{\mu_w} \exp[-0.013\rho_i(1-\phi)], \quad (5)$$

where  $d_i$  is the ice grain diameter, which we assume constant,  $g$  is the gravitational acceleration, and  $\mu_w$  is the water dynamic viscosity, which we assume constant. Note that the dry snow density ( $\rho_{\text{snow}}$ ) and porosity are related by the expression  $\rho_{\text{snow}} = \rho_i(1-\phi)$ , which appears in the exponential argument in Eq. (5). We assume the relative permeability is a convex function of saturation (Bear, 1972; Brooks & Corey, 1966) defined as

$$k_r(S) = \left( \frac{S - S_r}{1 - S_r} \right)^a, \quad (6)$$

where  $S_r$  is the irreducible water saturation and the parameter  $a > 1$  varies for different types of snow. The irreducible water saturation in subfreezing snow is approximately zero.  $S_r$  values slightly higher than zero could represent pre-melted water (Hansen-Goos & Wettlaufer, 2010; Slater & Michaelides, 2019) at temperatures below the melting point. Eq. (6) displays the same trend as the Genuchten-Mualem model (Mualem, 1976). Finally, the flow potential accounts for gravitational and capillary forces and is defined as

$$\Pi(S) = z - \psi(S) - \sqrt{\kappa}\nabla \cdot (\sqrt{\kappa}\nabla S), \quad (7)$$

where the first and second terms constitute the classical Richards model for unsaturated flow, while the third term is a non-local (also known as second-gradient) term associated with a macroscopic surface tension effect that gives rise to an unstable infiltration front and the emergence of gravity fingering (Cueto-Felgueroso & Juanes, 2008, 2009b). In Eq. (7), the  $z$ -coordinate increases with height,  $\psi$  is the Leverett J-function which accounts for capillary pressure, and  $\kappa$  is the expansion coefficient for the second-gradient theory (Beljadid et al., 2020). The functions  $\psi(S)$  and  $\kappa(S)$  are defined as

$$\psi(S) = h_{\text{cap}} S^{-\frac{1}{\alpha}} \left\{ 1 - \exp[\beta(S - \nu_e)] \left( 1 + \beta \frac{\alpha}{\alpha - 1} S \right) \right\}, \quad (8)$$



$$\kappa(S) = h_{\text{cap}}^2 \int_0^S \psi(S) \, dS = h_{\text{cap}}^3 \frac{\alpha}{\alpha - 1} S^{\frac{\alpha-1}{\alpha}} \{1 - \exp[\beta(S - \nu_e)]\}, \quad (9)$$

where  $h_{\text{cap}}$ ,  $\alpha$ ,  $\beta$ , and  $\nu_e$  are constants. The parameters  $h_{\text{cap}}$ ,  $\alpha$ ,  $\beta$ , and  $\nu_e$ , which may take different values for different types of snow, can be calibrated from water retention curves obtained from experiments or other models (Yamaguchi et al., 2010, 2012; Kat-sushima et al., 2013).

**Remark:** The relative permeability and the Leverett J-function (Eqs. (6) and (8)) account for infiltration through fixed porous microstructures. Due to the lack of information about the evolution of these hydraulic properties as the snow microstructure changes, we assume that the parameters involved in Eqs. (6) and (8) are constant during melt-water infiltration and refreezing.

## 2.2 Thermal balance

The evolution equations for the thermal energy in the ice and water phases are expressed as:

$$\rho_i c_{p,i} \frac{\partial[(1 - \phi)T_i]}{\partial t} = \nabla \cdot (K_i(1 - \phi)\nabla T_i) - \alpha_i \rho L_{\text{sol}} R_m W_{\text{SSA}}(T_{\text{int}} - T_{\text{melt}}) \quad (10)$$

$$\rho_w c_{p,w} \left[ \frac{\partial(\phi S T_w)}{\partial t} + \nabla \cdot (\mathbf{u} T_w) \right] = \nabla \cdot (K_w \phi S \nabla T_w) - \alpha_w \rho L_{\text{sol}} R_m W_{\text{SSA}}(T_{\text{int}} - T_{\text{melt}}), \quad (11)$$

where  $c_{p,i}$  is the specific heat capacity of ice and  $K_i$  and  $K_w$ , which we assume constant, are the ice and water thermal conductivity, respectively. The value of  $\rho$  depends on the direction of the phase transition such that  $\rho = \rho_w$  in case of freezing or  $\rho = \rho_i$  in case of melting. The coefficient  $\alpha_i$  (respectively,  $\alpha_w$ ) represents the percentage of latent heat released (or absorbed) by the ice phase (respectively, water phase) due to ice-water phase transitions. Note that  $\alpha_i + \alpha_w = 1$ . The estimation of  $\alpha_i$  and  $\alpha_w$  is described in the following section. Due to the lower density and specific heat capacity of air, we assume that heat exchange occurs only between ice and water.

### 2.2.1 Interfacial temperature $T_{\text{int}}$ and latent heat partition

We resort to a pore-scale solidification model (i.e., the generalized Stefan problem; see Gomez et al. (2019)) to estimate the temperature at the ice-water interface ( $T_{\text{int}}$ ) and the amount of latent heat partitioned to the ice and water phases ( $\alpha_i$  and  $\alpha_w$ ). Sharp-interface models of solidification such as the generalized Stefan problem usually consider

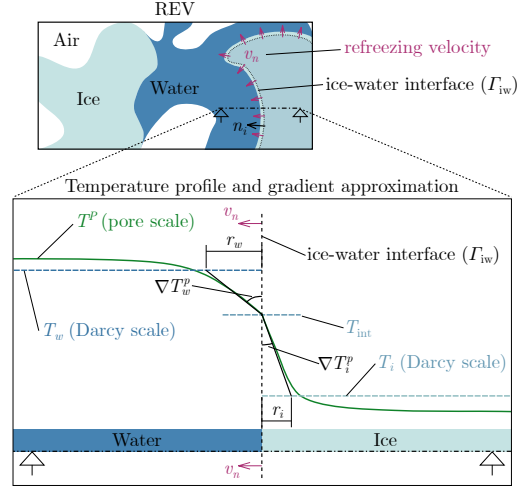


**Figure 2.** Approximation of the pore-scale temperature gradients on the ice-water interface ( $\Gamma_{iw}$ ). Ice and water pore-scale temperature gradients ( $\nabla T_i^P$  and  $\nabla T_w^P$ ) can be estimated from the Darcy-scale temperatures  $T_i$  and  $T_w$ , the ice-water interface ( $\Gamma_{iw}$ ) temperature  $T_{\text{int}}$ , and the characteristic lengths  $r_i$  and  $r_w$ . The parameters  $r_i$  and  $r_w$  can be calibrated from experimental data or pore-scale numerical simulations.

the following conditions on the moving ice-water interface, denoted as  $\Gamma_{iw}$ :

$$T_{\text{int}}^P = T_i^P \Big|_{\Gamma_{iw}} = T_w^P \Big|_{\Gamma_{iw}}, \quad (12)$$

$$K_i \nabla T_i^P \Big|_{\Gamma_{iw}} \cdot \mathbf{n}_i - K_w \nabla T_w^P \Big|_{\Gamma_{iw}} \cdot \mathbf{n}_i = L_{\text{sol}} \rho v_n, \quad (13)$$

$$\frac{T_{\text{int}}^P - T_{\text{melt}}}{L_{\text{sol}}/c_{p,w}} = -d_0 \chi - \beta_{\text{sol}} v_n, \quad (14)$$

where  $T_{\text{int}}^P$ ,  $T_i^P$  and  $T_w^P$  are the pore-scale temperatures (denoted using superscript  $P$ ) at the ice-water interface, within the ice phase, and within the water phase, respectively. Eq. (12) imposes temperature continuity at the interface. Eq. (13) accounts for the thermal energy conservation across  $\Gamma_{iw}$ . Eq. (14) is known as the Gibbs-Thomson condition and relates the velocity ( $v_n$ ), curvature ( $\chi$ ), and temperature ( $T_{\text{int}}^P$ ) of the interface. In Eq. (13),  $\mathbf{n}_i$  is the outwards unit normal vector of the ice phase pointing toward the water phase (see Fig. 2),  $v_n$  is the normal velocity of the interface (positive for ice growth), and  $\rho = \rho_w$  during freezing or  $\rho = \rho_i$  during melting. In Eq. (14), the parameter  $d_0$  is the capillary length and  $\chi$  is the interface curvature (positive for spherical ice grains).

To upscale the pore-scale solidification process defined by Eqs. (12)–(14) to the Darcy scale, we integrate Eqs. (13) and (14) along  $\Gamma_{iw}$  in a REV, which results in the expres-

sions:

$$K_i \overline{\nabla T_i^P} \Big|_{\Gamma_{iw}} - K_w \overline{\nabla T_w^P} \Big|_{\Gamma_{iw}} = L_{\text{sol}} \rho \overline{v_n}, \quad (15)$$

$$\frac{\overline{T_{\text{int}}^P} - T_{\text{melt}}}{L_{\text{sol}}/c_{p,w}} = -\beta_{\text{sol}} \overline{v_n}, \quad (16)$$

where we define the volume-averaged quantities:

$$\overline{\nabla T_i^P} \Big|_{\Gamma_{iw}} = \frac{\int_{\Gamma_{iw}} \nabla T_i^P \cdot \mathbf{n}_i \, da}{\int_{\Gamma_{iw}} da}, \quad \overline{\nabla T_w^P} \Big|_{\Gamma_{iw}} = \frac{\int_{\Gamma_{iw}} \nabla T_w^P \cdot \mathbf{n}_i \, da}{\int_{\Gamma_{iw}} da}, \quad (17)$$

$$\overline{v_n} = \frac{\int_{\Gamma_{iw}} v_n \, da}{\int_{\Gamma_{iw}} da}, \quad \overline{T_{\text{int}}^P} = \frac{\int_{\Gamma_{iw}} T_{\text{int}}^P \, da}{\int_{\Gamma_{iw}} da} = T_{\text{int}}, \quad \overline{\chi} = \frac{\int_{\Gamma_{iw}} \chi \, da}{\int_{\Gamma_{iw}} da} \approx 0. \quad (18)$$

Note that  $\overline{T_{\text{int}}^P}$  is the equivalent Darcy-scale interface temperature  $T_{\text{int}}$  (assumed constant in the REV). We assume that the volume-averaged curvature of the ice-water interface  $\overline{\chi}$  is zero. In addition, we note that, during meltwater refreezing for typical values of ice grain curvature and temperature,  $|d_0 \chi| \ll |(T_{\text{int}}^P - T_{\text{melt}}) c_{p,w} / L_{\text{sol}}|$ . Thus, we neglect the  $d_0 \chi$  contribution to the interface dynamics when upscaling from Eq.14 to Eq.16.

To estimate temperature gradients across the interface, we assume that the pore-scale temperature varies linearly between the interface temperature  $T_{\text{int}}$  and the Darcy-scale temperature of the corresponding phase ( $T_i$  or  $T_w$ ) over a finite thermal diffusion length ( $r_i$  or  $r_w$ ). We illustrate this approximation in Fig. 2, which yields the following expressions:

$$\overline{\nabla T_i^P} \Big|_{\Gamma_{iw}} = \frac{T_{\text{int}} - T_i}{r_i}, \quad \overline{\nabla T_w^P} \Big|_{\Gamma_{iw}} = \frac{T_w - T_{\text{int}}}{r_w}. \quad (19)$$

Combining Eqs. (15) and (16) and the temperature gradient approximation defined in Eq. (19), we can write  $T_{\text{int}}$  as a function of  $T_i$  and  $T_w$ :

$$T_{\text{int}}(T_i, T_w) = \frac{\frac{c_{p,w}}{L_{\text{sol}}} T_{\text{melt}} + \frac{\beta_{\text{sol}} K_i}{\rho L_{\text{sol}} r_i} T_i + \frac{\beta_{\text{sol}} K_w}{\rho L_{\text{sol}} r_w} T_w}{\frac{c_{p,w}}{L_{\text{sol}}} + \frac{\beta_{\text{sol}} K_i}{\rho L_{\text{sol}} r_i} + \frac{\beta_{\text{sol}} K_w}{\rho L_{\text{sol}} r_w}}. \quad (20)$$

The parameters  $r_i$  and  $r_w$  can be estimated from pore-scale simulations, experimental observations, or field data. Here, we calibrate  $r_i$  and  $r_w$  with numerical results of a pore-scale solidification model, whose details are included in the Appendix. Based on the pore-scale model, we take  $r_i = 0.06 d_i$  and  $r_w = 1.35 r_i$ .

The ice and water phases absorb or release latent heat during ice-water phase transitions. We denote the amount of thermal energy absorbed or released by phase  $j$  in the REV as  $H_j$ , which can be computed with the integral

$$H_j = \int_{\Gamma_{iw}} K_j \nabla T_j^P \cdot \mathbf{n}_j \, da, \quad (21)$$

where the index  $j$  stands for  $i$  (ice) or  $w$  (water) and  $\mathbf{n}_w$  is the outward normal vector to the water phase, such that  $\mathbf{n}_w = -\mathbf{n}_i$ . The total amount of latent heat absorbed (or released) is  $H_i + H_w$ , which results from integrating Eq. (13) along  $\Gamma_{iw}$  in the REV. The latent heat partition can be estimated according to the relative thermal flux of each phase at the interface. Therefore, we can define the coefficients  $\alpha_i = H_i / (H_i + H_w)$  and  $\alpha_w = H_w / (H_i + H_w)$ ; see Eqs. (10) and (11). Using Eqs. (17) and (19), we can approximate  $\alpha_i$  and  $\alpha_w$  as

$$\alpha_i = \frac{K_i \frac{T_{\text{int}} - T_i}{r_i}}{K_w \frac{T_{\text{int}} - T_w}{r_w} + K_i \frac{T_{\text{int}} - T_i}{r_i}}, \quad \alpha_w = \frac{K_w \frac{T_{\text{int}} - T_w}{r_w}}{K_w \frac{T_{\text{int}} - T_w}{r_w} + K_i \frac{T_{\text{int}} - T_i}{r_i}}. \quad (22)$$

### 3 Numerical implementation

#### 3.1 Strong form of the problem

We rearrange the equations presented in Section 2 in the following way. First, we split the flow potential (Eq. (7)) to consider the gravitational and capillary terms as separate variables such that  $\Pi(S) = z - \theta(S)$ . Then, we use Eqs. (20) and (22) to simplify Eqs. (10) and (11). The final equations we solve for are:

$$\frac{\partial \phi}{\partial t} = R_m W_{\text{SSA}} (T_{\text{int}} - T_{\text{melt}}), \quad (23)$$

$$\frac{\partial(\phi S)}{\partial t} - \frac{\partial}{\partial z} (K_s k_r) + \nabla \cdot (K_s k_r \nabla \theta) = \frac{\rho_i}{\rho_w} R_m W_{\text{SSA}} (T_{\text{int}} - T_{\text{melt}}), \quad (24)$$

$$\theta = \psi + \sqrt{\kappa} \nabla \cdot (\sqrt{\kappa} \nabla S), \quad (25)$$

$$\frac{\partial[(1 - \phi)T_i]}{\partial t} = \nabla \cdot (D_i(1 - \phi) \nabla T_i) + W_{\text{SSA}} D_i \frac{T_{\text{int}} - T_i}{r_i}, \quad (26)$$

$$\frac{\partial(\phi S T_w)}{\partial t} - \frac{\partial}{\partial z} (K_s k_r T_w) + \nabla \cdot (K_s k_r T_w \nabla \theta) = \nabla \cdot (D_w \phi S \nabla T_w) + W_{\text{SSA}} D_w \frac{T_{\text{int}} - T_w}{r_w}, \quad (27)$$

where  $D_i = K_i / (\rho_i c_{p,i})$  and  $D_w = K_w / (\rho_w c_{p,w})$  are the ice and water thermal diffusion coefficients, respectively. Eq. (25) defines an additional problem unknown,  $\theta(\mathbf{x}, t)$ , which represents the capillary effects in the flow potential.

##### 3.1.1 Boundary conditions, initial conditions, and parameter values

We solve the model equations in a 1D vertical domain ( $\Omega_{1D}$ , along the  $z$  axis) and a 2D rectangular domain ( $\Omega_{2D}$ , in the  $xz$  plane). In  $\Omega_{1D}$  and  $\Omega_{2D}$ , we denote the top and bottom boundaries as  $\Gamma_t$  and  $\Gamma_b$ , respectively. In  $\Omega_{2D}$ , we denote the lateral boundaries as  $\Gamma_l$ . If we denote the outward normal to the boundary as  $\mathbf{n}$ , the boundary conditions

227 read

$$\mathbf{u} \cdot \mathbf{n} = 0, \quad D_i(1 - \phi)\nabla T_i \cdot \mathbf{n} = 0, \quad (D_w\phi S\nabla T_w - \mathbf{u}T_w) \cdot \mathbf{n} = 0 \quad \text{on } \Gamma_l, \quad (28)$$

$$\mathbf{u} \cdot \mathbf{n} = -u_{\text{top}}(x, t), \quad T_i = T_{\text{melt}}, \quad T_w = T_{\text{melt}} \quad \text{on } \Gamma_t, \quad (29)$$

$$\mathbf{u} \cdot \mathbf{n} = K_s(\phi)k_r(S), \quad T_i = T_{i,\text{bot}}, \quad (D_w\phi S\nabla T_w - \mathbf{u}T_w) \cdot \mathbf{n} = 0 \quad \text{on } \Gamma_b, \quad (30)$$

228 along with the zero flux condition  $\nabla S \cdot \mathbf{n} = 0$  on the entire boundary. These bound-  
 229 ary conditions assume a closed domain for heat and melt flux in the lateral direction;  
 230 a fixed meltwater influx through the top boundary ( $u_{\text{top}}$ ); water and ice temperatures  
 231 equal to the freezing point ( $T_{\text{melt}}$ ) at the top boundary; a fixed ice temperature ( $T_{i,\text{bot}}$ )  
 232 on the bottom boundary, and free water flow and temperature fluxes through the bot-  
 233 tom boundary. For the 2D simulations shown in this work, we assume that  $u_{\text{top}}$  is fixed  
 234 in time and displays a mild Gaussian spatial perturbation (with mean  $\overline{u_{\text{top}}}$  and standard  
 235 deviation  $\overline{u_{\text{top}}} \times 10^{-3}$ ) to accelerate the emergence of flow instabilities (Cueto-Felgueroso  
 236 & Juanes, 2009b). We do not explicitly account for solar radiation in our model; instead,  
 237 we impose a meltwater generation rate at the top boundary due to ice melting.

238 The parameter values for the general properties of the snowpack and the meltwa-  
 239 ter are listed in Table 1. The parameters that depend on the snow type or that vary for  
 240 each example are defined in the corresponding subsection in Table 2 in Section 4.

241 Unless otherwise stated, we consider an initially dry homogeneous snowpack with  
 242 uniform  $\phi$ ,  $K_s$ ,  $\text{SSA}_0$ , and  $T_i$ . The initial conditions are:  $\phi(\mathbf{x}, 0) = \phi_0$ ,  $S(\mathbf{x}, 0) = 10^{-3}$ ,  
 243  $T_i(\mathbf{x}, 0) = T_{i,0}$ , and  $T_w(\mathbf{x}, 0) = T_{\text{melt}}$ , where the small amount of initial saturation rep-  
 244 represents pre-melted water imposed for regularization purposes (see Section *Regularity of*  
 245 *functions*  $W_{\text{SSA}}$ ,  $k_r$ ,  $\psi$ , and  $\kappa$  in Appendix). Note that the initial porosity  $\phi_0$  can be es-  
 246 timated from the dry snow density  $\rho_{\text{snow}}$  as  $\phi_0 = 1 - \rho_{\text{snow}}/\rho_i$ . We estimate  $\text{SSA}_0$  with  
 247 the empirical expression proposed in Domine et al. (2007), which relates the snow SSA  
 248 and the snow density.

### 249 3.2 Spatial and time discretization

250 We use isogeometric analysis (Hughes et al., 2005), a finite element method that  
 251 employs B-splines as basis functions, to solve the problem. We derive the weak form of  
 252 the problem by multiplying Eqs. (23)–(27) with weighting functions, integrating over the  
 253 domain, and integrating by parts considering the boundary conditions defined above. We

Parameter	Description	Value	Units
$\rho_i$	Ice density	919	$\text{kg m}^{-3}$
$\rho_w$	Water density	1000	$\text{kg m}^{-3}$
$c_{p,i}$	Ice specific heat capacity	$1.96 \times 10^3$	$\text{J kg}^{-1} \text{C}^{-1}$
$c_{p,w}$	Water specific heat capacity	$4.2 \times 10^3$	$\text{J kg}^{-1} \text{C}^{-1}$
$L_{\text{sol}}$	Solidification latent heat	$3.34 \times 10^5$	$\text{J kg}^{-1}$
$\beta_{\text{sol}}$	Kinetic attachment coefficient	$\sim 800$	$\text{s m}^{-1}$
$K_i$	Ice thermal conductivity	2.29	$\text{W m}^{-1} \text{C}^{-1}$
$K_w$	Water thermal conductivity	0.554	$\text{W m}^{-1} \text{C}^{-1}$
$T_{\text{melt}}$	Freezing point	0	$^{\circ}\text{C}$
$g$	Gravitational acceleration	9.81	$\text{m s}^{-2}$
$\mu_w$	Water dynamic viscosity	$1.792 \times 10^{-3}$	$\text{kg m}^{-1} \text{s}^{-1}$

**Table 1. Key model parameters and their values.** See Table 2 for additional parameters and their values for different types of snow.

obtain the Galerkin form by substituting the unknowns and weighting functions with discrete approximations. Although we could use linear (bilinear in 2D) basis functions for the spatial discretization, we opted for employing quadratic  $\mathcal{C}^1$ -continuous B-splines, which provide more stable solutions. Note that there are very small non-physical oscillations in  $S$  (also called undershoot) located downstream the wetting front (Cueto-Felgueroso & Juanes, 2009a; Gomez et al., 2013). These oscillations might affect the accuracy of the solution (Gomez et al., 2013). Here, we reduce the oscillations by using quadratic B-splines and a fine mesh. We find that the influence of these minor oscillations on the overall infiltration pattern is minimal. In addition, we redefine the functions  $k_r$ ,  $\psi$ ,  $\kappa$ , and  $W_{\text{SSA}}$  to avoid singularities when  $S \leq 0$ ; see more details in Appendix.

For the time integration, we use the generalized- $\alpha$  method (Chung & Hulbert, 1993; Jansen et al., 2000) with an adaptive time stepping scheme based on the number of Newton-Raphson iterations. To perform the simulations, we develop a code on top of the open source libraries PETSc (Balay et al., 2022) and PetIGA (Dalcin et al., 2016).

## 4 Results

In this section, we first present results of model validation against existing data. Then, we present 2D simulations of melt infiltration into homogeneous snow. In the examples shown here, we consider two types of scenarios: isothermal and non-isothermal meltwater infiltration. In the isothermal case, the ice and water temperatures are fixed to the melting point and phase change does not occur. For the isothermal examples shown in this section we solve equations (24) and (25) only, where we neglect the right-hand side of Eq. (24) (more details in Appendix). In the non-isothermal case, a portion of the meltwater refreezes because the snow is below the freezing point.

### 4.1 Model validation against existing data in 1D

In this section we validate our model against existing experimental and field data. First, we test our model under isothermal conditions and compare against laboratory experiments of water infiltration in a snow column. Then, we perform non-isothermal simulations that mimic field conditions reported in Humphrey et al. (2012), and compare the temperature profile of a 10 m snow column during melt infiltration and refreezing events.

#### 4.1.1 Capillary pressure dynamics during isothermal infiltration

Darcy-scale models of meltwater infiltration rely on knowing the hydraulic properties of the snowpack. These properties include the relative permeability  $k_r$ , the saturated hydraulic conductivity  $K_s$ , and the water retention curve (WRC,  $\psi$  in our model), which vary for each type of snow. Recent studies have experimentally measured these hydraulic properties of snow under isothermal conditions (Yamaguchi et al., 2010; Katsushima et al., 2013; Avanzi et al., 2016), where a constant water influx (at  $T = 0^\circ\text{C}$  to ensure no refreezing) is introduced at the top surface of a snow column. In particular, Katsushima et al. (2013) estimated the hydraulic conductivity, the van Genuchten (Van Genuchten, 1980) and Genuchten-Mualem (Mualem, 1976) model parameters of the WRC and the relative permeability for four different types of snow, namely,  $S_S$ ,  $S_M$ ,  $S_L$ , and  $S_{LL}$  (in the order ascending ice grain size). The authors also measured the capillary pressure head 2 cm below the surface of the snow for three different water influx rates. The results display a capillary pressure overshoot during meltwater infiltration in

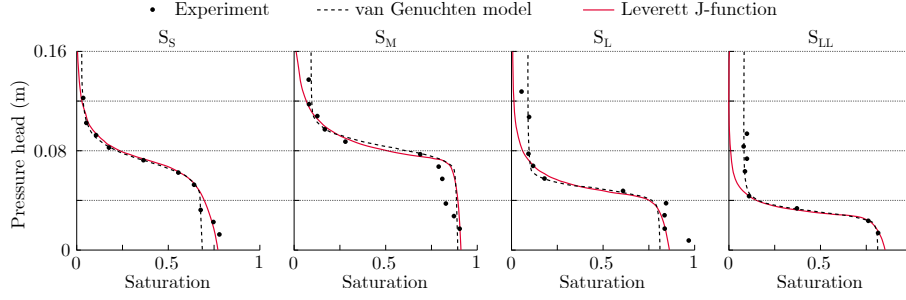


**Figure 3. Imbibition WRCs for snow types  $S_S$ ,  $S_M$ ,  $S_L$ , and  $S_{LL}$ .** Experimentally observed (dots) and the estimated van Genuchten model (dashed line) WRCs during imbibition taken from Katsushima et al. (2013). Note that Katsushima et al. (2013) reported the drainage WRC, which is approximately twice the imbibition WRC (Leroux & Pomeroy, 2017). The pressure head plotted here is half the pressure head reported in Katsushima et al. (2013). We use least square analysis to calibrate the Leverett J-function (Eq. (8), solid red line) from the experimental data. We assume a null irreducible water saturation to account for infiltration in subfreezing scenarios and, for simplicity, we take  $\nu_e = 1$ . Note the Leverett J-function in our model represents the imbibition WRC. The values of  $h_{cap}$ ,  $\alpha$ , and  $\beta$  are listed in Table 2.

298 snow (see Fig. 4, dashed lines). Indeed, capillary pressure overshoot, indicating a higher  
 299 water saturation at the wetting front compared to the saturation upstream, is a signa-  
 300 ture and a necessary condition for preferential flow (Geiger & Durnford, 2000; Eliassi &  
 301 Glass, 2003; DiCarlo, 2004, 2013). Here, we use our model to replicate the experiments  
 302 in Katsushima et al. (2013) to reproduce the capillary pressure overshoot. Since we use  
 303 the Leverett J-function instead of the van Genuchten model to represent the WRC, we  
 304 need to recalibrate the model parameters used in Eq. (8) for each type of snow (Fig. 3).  
 305 We use the Mualem-Genuchten model for relative permeability to calibrate the param-  
 306 eter  $a$  in Eq. (6). Table 2 lists the parameter values from the calibration as well as the  
 307 snow density, hydraulic conductivity, and ice grain size for the four types of snow (val-  
 308 ues taken from Katsushima et al. (2013)).

309 Based on the experiments in Katsushima et al. (2013), we consider a 25 cm-deep  
 310 1D domain, discretized with 300 elements, and assume uniform  $K_s$  (see Table 2). We  
 311 run three simulations for each type of snow, corresponding to the three water influx rates  
 312 ( $u_{top}$ ) injected in Katsushima et al. (2013). We measure the saturation 2 cm below the  
 313 top boundary, which we denote as  $S_C$ , and compute the corresponding capillary pres-



Snow type	$\rho_{\text{snow}}$ (kg/m <sup>3</sup> )	$K_s$ (cm/min)	$d_i$ (mm)	$h_{\text{cap}}$ (m)	$\alpha$ (-)	$\beta$ (-)	a (-)
S <sub>S</sub>	387	4.764	0.231	0.06	5	11	2.8
S <sub>M</sub>	489	5.298	0.421	0.07	5	46	2.7
S <sub>L</sub>	512	9.828	1.049	0.04	4	24	2.7
S <sub>LL</sub>	501	32.220	1.439	0.025	4	22	2.8

**Table 2.** Parameter values used to replicate experiments in Katsushima et al.

(2013). We consider a null irreducible water saturation ( $S_r = 0$ ), and assume  $\nu_e = 1$ .

sure head as  $\theta(S_C) = \psi(S_C) + \sqrt{\kappa} \nabla \cdot (\sqrt{\kappa} \nabla S_C)$ . Figure 4 shows the time evolution of  $\theta(S_C)$  for snow types S<sub>M</sub> (top row), S<sub>L</sub> (center row), and S<sub>LL</sub> (bottom row) and for low (left column), medium (center column), and high (right column)  $u_{\text{top}}$ . We set  $t = 0$  min as the time when the infiltration front reaches the measurement point. We do not include snow type S<sub>S</sub> here as the experiments do not exhibit pressure head overshoot.

The results show that our model is able to reproduce the overall dynamics of capillary pressure during infiltration into a homogeneous snowpack. Specifically, we indicate the time for the minimum pressure based on the 1D simulations (denoted as  $t_{\text{ov}}^S$ ) and the experiments (denoted as  $t_{\text{ov}}^E$ ), which exhibit good agreement for most of the snow types and inflow rates. The 1D results also show a good agreement in the pressure values for snow types S<sub>L</sub> and S<sub>LL</sub>, while the match is worse for snow types S<sub>M</sub> and S<sub>S</sub> (results not shown).

#### 4.1.2 Rate of infiltration under isothermal conditions

Avanzi et al. (2016) experimentally investigated unstable infiltration at 0 °C (isothermal conditions) into a snow column composed of a layer of finer snow on top of a layer of coarser snow. The authors performed experiments in which they used different types of snow, namely, fine (F), medium (M), and coarse (C), and different influx rates. These experiments demonstrate both unstable infiltration and melt ponding at the layer interface. Some of the data analyzed includes the infiltration speed and the ponding layer thickness. Here, we focus on comparing the measured infiltration speed and leave the ponding effect for future research. Thus, we focus on the infiltration through the upper layer of the snow column before meltwater reaches the layer interface. In our simulations, we

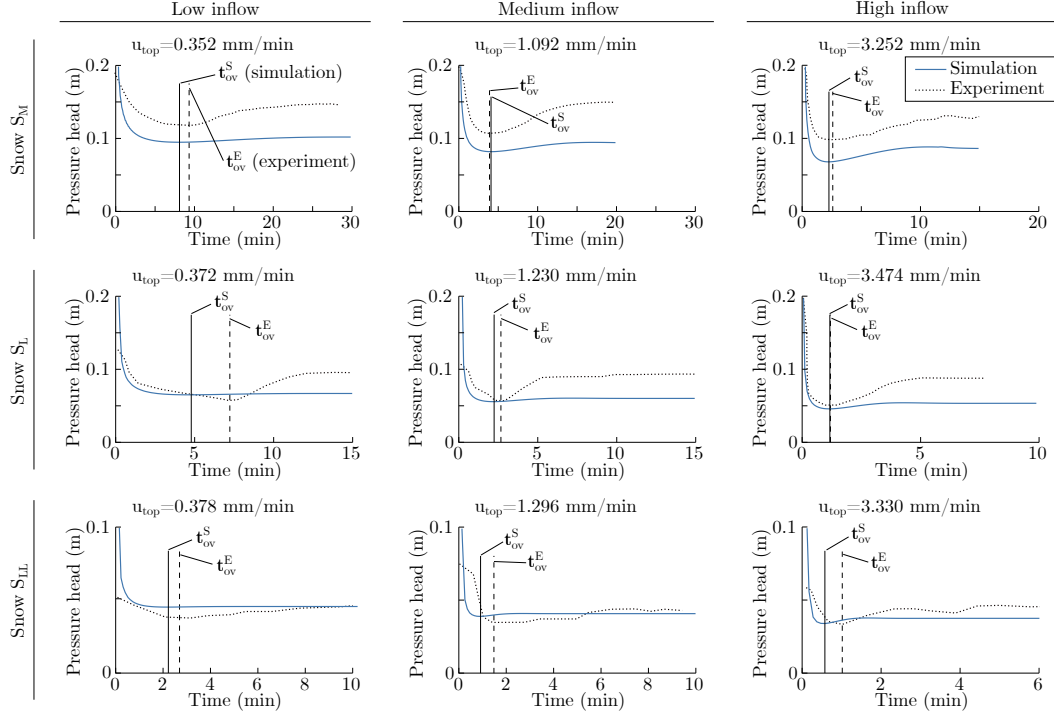


**Figure 4. Capillary pressure dynamics from snow experiments and 1D simulations.**

Time evolution of the pressure head measured 2 cm below the top surface of the snow column corresponding to snow types  $S_M$  (top row),  $S_L$  (middle row), and  $S_{LL}$  (bottom row) for low (left column), medium (middle column), and high (right column) meltwater influx rates. The solid blue line represents our model results, while the dashed black line represents the experiments in Katsushima et al. (2013).  $t_{ov}^S$  and  $t_{ov}^E$  indicate the time for minimum pressure head in our simulations and the experiments, respectively.

consider a 1D vertical domain of 10 cm discretized with 200 elements, which has the same height as the upper layer of snow in Avanzi et al. (2016). We assume an initially uniform snow column with constant porosity/density (Table 3). As done in Hirashima et al. (2017), we assume that snow types F and M in Avanzi et al. (2016) have the same properties as snow types  $S_M$  and  $S_{LL}$  in Katsushima et al. (2013), respectively. Thus, we use the hydraulic properties of snow types  $S_M$  and  $S_{LL}$  defined in Table 2 except for  $K_s$ , which we estimate with Eq. (5). The snow type, snow density, and meltwater influx rate for each experiment are listed in Table 3.

We use our model to estimate the arrival time ( $t_a$ ) of the infiltration front to the interface, and we compare with the arrival time in the experiments  $t_a^A$  (Avanzi et al., 2016)

Exper.	Snow	$\rho_{\text{snow}}$	$u_{\text{top}}$	$t_a$ (this work)	$t_a^A$ (Avanzi)	$t_a^H$ (Hirashima)
FC1	S <sub>M</sub>	417 kg/m <sup>3</sup>	0.198 mm/min	19.4 min	34.8 min	16.7 min
FC2	S <sub>M</sub>	449 kg/m <sup>3</sup>	0.466 mm/min	12.7 min	15.2 min	8.7 min
FC3	S <sub>M</sub>	433 kg/m <sup>3</sup>	1.883 mm/min	5.0 min	7.1 min	4.0 min
FM1	S <sub>M</sub>	444 kg/m <sup>3</sup>	0.198 mm/min	20.9 min	20.0 min	17.0 min
FM2	S <sub>M</sub>	442 kg/m <sup>3</sup>	0.462 mm/min	12.4 min	11.3 min	10.7 min
FM3	S <sub>M</sub>	455 kg/m <sup>3</sup>	1.833 mm/min	5.5 min	6.7 min	4.3 min
MC1	S <sub>LL</sub>	472 kg/m <sup>3</sup>	0.183 mm/min	10.5 min	5.3 min	9.0 min
MC2	S <sub>LL</sub>	498 kg/m <sup>3</sup>	0.455 mm/min	6.3 min	3.0 min	4.7 min
MC3	S <sub>LL</sub>	494 kg/m <sup>3</sup>	1.850 mm/min	2.5 min	0.8 min	1.7 min

**Table 3. Arrival time for isothermal infiltration.** Each row represents a different experiment. We indicate the upper layer snow type, snow density, and the meltwater influx rate for each experiment. The parameter values for snow types S<sub>M</sub> and S<sub>LL</sub> are listed in Table 2. We set  $d_i = 0.41$  mm and  $d_i = 1.5$  mm for snow types S<sub>M</sub> and S<sub>LL</sub>, respectively. We indicate the arrival time computed with our model ( $t_a$ ), observed in the experiments ( $t_a^A$ , see Avanzi et al. (2016)), and computed in Hirashima et al. (2017) ( $t_a^H$ ).

and the simulated arrival time  $t_a^H$  by the same authors in Hirashima et al. (2017) (see Table 3). Our model provides a good approximation for experiments FM (center rows), while it underestimates the arrival time for experiments FC (three top rows in the table), and overestimates  $t_a$  for experiments MC (three bottom rows in the table). Compared to Hirashima et al. (2017), our model provides a better estimation of the arrival time for experiments FC and FM, while our estimation is worse for experiments MC. There are two main sources of error in our numerical results. First, the hydraulic properties of the snow used in Avanzi et al. (2016) are taken from those of a separate experiment (Katsushima et al., 2013) and, thus, may be inaccurate. Second, 1D simulations are unable to capture the effect of unstable infiltration on arrival time. As we show in Section 4.2, preferential infiltration in 2D exhibits channelized flows with enhanced infiltration speed.

**Remark:** We also run 2D simulations in a rectangular domain ( $5\text{ cm(w)} \times 10\text{ cm(h)}$ ), which corresponds to the diameter and height of the snow column used in the experiments (Avanzi et al., 2016). Using the parameters in Table 2 for snow  $S_M$  and  $S_{LL}$ , the 2D simulations show capillary pressure overshoot but do not exhibit preferential infiltration, contrary to experimental observation. We hypothesize that the disagreement here is because the characteristic finger width prescribed by the simulation parameters (e.g.  $h_{\text{cap}}$  and  $a$ ) is larger than the domain width. To observe preferential infiltration in a 5 cm wide domain for  $S_M$  and  $S_{LL}$  snow type, smaller values of  $h_{\text{cap}}$  and/or larger values of  $a$  must be employed in our model.

#### 4.1.3 *Non-isothermal infiltration: meltwater refreezing*

When meltwater infiltrates into subfreezing snow, it leads to melt refreezing. At the macroscopic scale, refrozen melt structures have been readily observed in the field at the scale of meters to kilometers (Humphrey et al., 2012; Lazzaro et al., 2015; Culberg et al., 2021). Horizontal refrozen structures are low permeability regions in snowpack that hinder downward percolation, promote lateral runoff (Culberg et al., 2021; Clerx et al., 2022), and play an important role in snow hydrology.

To validate our model’s ability to capture the thermal dynamics during melt infiltration and refreezing, we compare results with a recent field study by Humphrey et al. (2012). This study collected temperature profiles along 10 m deep snowpack columns in the Greenland accumulation region and recorded the thermal signatures of meltwa-

ter infiltration and refreezing events during annual melt cycles. Among other results, the authors provided temperature profiles at site T2 (see location in Humphrey et al. (2012)) during an 18 day interval in the summer of 2007 in Greenland (Fig. 5A). The data shows a gradual increase in the snow temperature towards the surface due to the infiltration of meltwater and the latent heat released due to melt refreezing. Spikes observed at days 199 and 200 are likely caused by heterogeneous meltwater infiltration and suggest the presence of channelized flow (ice pipes) that delivers melt to deeper points or a lateral flux of water along ice lenses, causing a local increase in the snow temperature.

Here, we use our model to replicate the meltwater infiltration and refreezing process observed in Humphrey et al. (2012). We consider a 1D vertical domain of 9 m meshed with 3600 elements which represents the snowpack column from 1 m to 10 m deep. The approximate snow density is reported in Humphrey et al. (2012) as  $\rho_{\text{snow}} = 375 \text{ kg m}^{-3}$ , which has similar density to snow type S<sub>S</sub> (Table 2). Hence, we assume the hydraulic properties of snow type S<sub>S</sub> for this field site and compute the snow hydraulic conductivity with Eq. 5. As initial conditions, we consider a uniform porosity and SSA estimated from  $\rho_{\text{snow}}$ , yielding  $\phi = 0.5924$  and  $\text{SSA}_0 = 3514 \text{ m}^{-1}$  (Section 3.1.1). We consider the temperature profile observed in day 185 as the initial ice temperature in our simulations. We follow Meyer & Hewitt (2017) and assume a constant influx rate between days 185 and 197 ( $u_{\text{top},1}$ ), and a different and constant influx rate between days 197 and 203 ( $u_{\text{top},2}$ ). The exact values of  $u_{\text{top},1}$  and  $u_{\text{top},2}$  are calibrated such that the infiltration front (i.e., the deepest point where  $T_i \approx T_{\text{melt}}$ ) at days 197 and 203 match the observations, which yield  $u_{\text{top},1} = 0.129 \text{ mm/h}$  and  $u_{\text{top},2} = 0.526 \text{ mm/h}$ .

In Fig. 5B–E, we plot the simulated LWC, porosity, ice temperature, and water temperature profiles for the initial time (day 185) and days 197 and 203, and compare against the measured ice temperature profile (dashed lines in Fig. 5D). Despite the simplifying assumptions, our results show good agreement with the temperature profile observed in the field.

The simulated LWC, porosity, and water temperature results exhibit some of the main features of the LTNE assumption in our model. First, the porosity does not display a piecewise uniform distribution as predicted in Meyer & Hewitt (2017). For instance, the porosity distribution at day 203 (green line in Fig. 5C) shows a gradual decrease in porosity from 2 m to 3.5 m depth. A higher porosity at 2 m implies that less refreezing

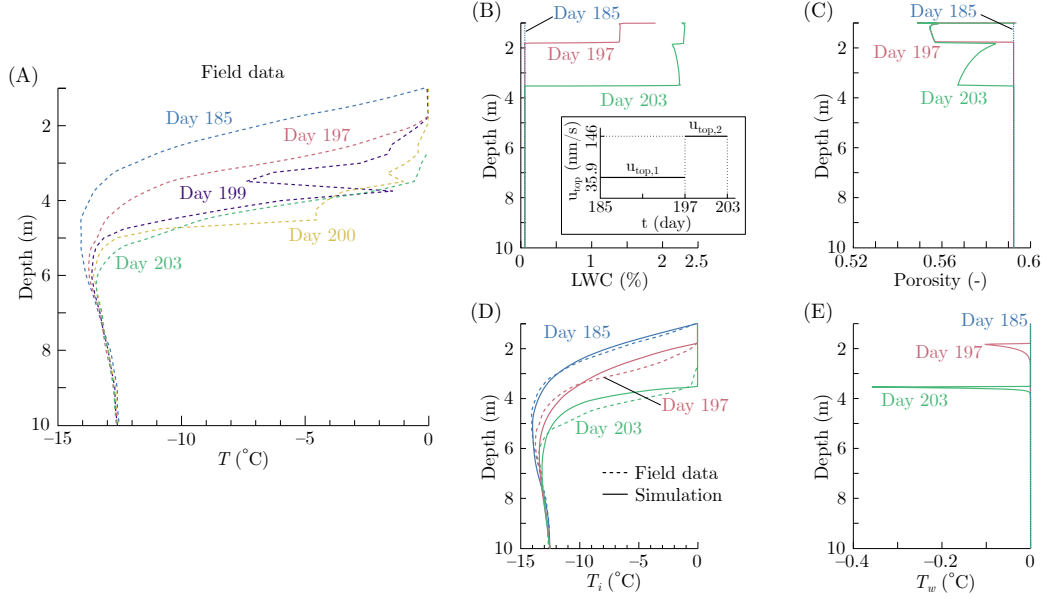


**Figure 5. Meltwater infiltration and refreezing during heating and cooling events.**

(A) Field data: Snow temperature profile measured in Humphrey et al. (2012) at days 185, 197, 199, 200, and 203 (adapted from Humphrey et al. (2012)). Simulation results: (B) LWC, (C) porosity, (D) ice temperature, and (E) water temperature profiles along the snow depth at days 185 (initial time, blue), 197 (red), and 203 (green). Dashed lines in (D) correspond to field data measured in Humphrey et al. (2012). The inset in (B) indicates the meltwater influx rate  $u_{\text{top}}$  as a function of time, which we assume piecewise constant.

has occurred, which can be attributed to (1) ice warming to the melting temperature sooner at such depth, and/or (2) differences in refreezing kinetics caused by local changes in  $T_{\text{int}}$  and  $W_{\text{SSA}}$ .

Second, our results display the undercooling of the liquid water due to the partitioning of the latent heat into the ice and water phases. Water undercooling is also captured in pore-scale simulations of water solidification (see Fig. 10B in Appendix). Unfortunately, we do not have available field or experimental data to validate the  $T_w$  results. Note that the undercooling peak is located just downstream the wetting front (Fig. 5E), where we numerically impede a total refreezing of water (we impose a minimum LWC  $\sim 10^{-3}$ ; see Section *Regularity of functions*  $W_{\text{SSA}}$ ,  $k_r$ ,  $\psi$ , and  $\kappa$  in Appendix). This may lead to the overestimation of the undercooling spike. We also ran simulations in which we disregard the latent heat partition by imposing  $\alpha_i = 1$  and  $\alpha_w = 0$  in Eqs. (10)

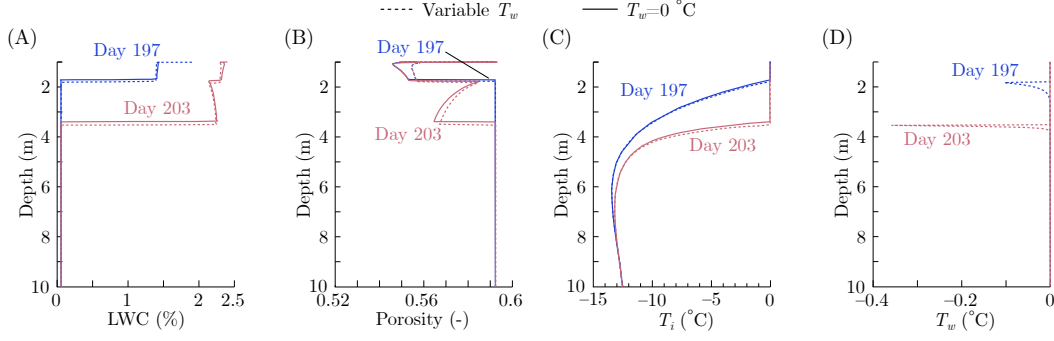


**Figure 6. Influence of the latent heat partition in meltwater infiltration and re-freezing.** (A) LWC, (B) porosity, (C) ice temperature, and (D) water temperature profiles along the snow depth at days 197 (blue) and 203 (red). Simulation results considering (dashed line) and neglecting (solid line) latent heat partition. We neglect the latent heat partition by imposing  $\alpha_i = 1$  and  $\alpha_w = 0$  in the  $T_i$  and  $T_w$  evolution equations; see Eqs. (10) and (11). We consider the same parameter values and influx rates as in Fig. 5.

and (11). In this case, the latent heat is entirely absorbed by the ice phase so that the water temperature remains at the melting point. In Fig. 6, we compare the results considering (dashed line) and neglecting (solid line) the latent heat partition and find that the infiltration speed is slightly lower and changes in porosity are slightly higher in case of neglecting the latent heat partition.

## 4.2 Isothermal preferential infiltration

The isothermal version of our model ( $T_i = T_w = 0^\circ\text{C}$ , thus solving only Eqs. (24)–(25)) is equivalent to that proposed by Cueto-Felgueroso & Juanes (2008), which was proposed to describe infiltration in soil. The reader is referred to Cueto-Felgueroso & Juanes (2008, 2009b); Cueto-Felgueroso et al. (2020a,b) for a more extensive analysis of the model. Here, we briefly discuss the results of isothermal infiltration, simulated with the proposed model applied to real snow properties. We run a simulation in a  $1\text{ m} \times 2\text{ m}$  domain, discretized with  $400 \times 800$  elements. We consider the hydraulic properties of the snow type S<sub>LL</sub> (Table 2) with  $d_i = 1.5\text{ mm}$  and  $K_s$  taken from Eq. (5). As mentioned in Section 4.1.2, we need to reduce  $h_{\text{cap}}$  and/or increase  $a$  (in Eqs. (6) and (8)) to produce fingers with cm-scale width observed in experiments and field. Here, we opted for increasing the relative permeability exponent  $a$  and take  $a = 5$ . We impose a con-

stant meltwater influx  $u_{\text{top}} = 0.6 \text{ mm/min}$ . In addition, we perform the equivalent simulation in 1D using the same parameter values, which will not capture unstable infiltration.

In Fig. 7A, we plotted the LWC distribution of the 2D simulation at five different times. The 2D results show the ability of our model to reproduce unstable flow through completely homogeneous snow with a constant meltwater influx. The perturbation corresponds to small-scale heterogeneities in natural environments. Numerically, if we do not include this perturbation, fingers would appear later in the simulation (at  $t \approx 60 \text{ min}$ ) and at a deeper point in the snowpack (results not shown). The fingering pattern appears as smooth vertical channels distributed with uniform spacing that preferentially conduct downward melt flow. In Fig. 7B, we compare the LWC profile of the 1D simulation (red line) with the horizontally averaged LWC of the 2D simulation (blue line). The results show that unstable infiltration in 2D delivers melt to deeper depths than stable infiltration would predict. We also note that the 1D results shown here illustrate the saturation overshoot at the infiltration front, while the 1D results in Section 4.3 do not (Fig. 5A). This is because the saturation overshoot depends on the melt influx rate and the parameters values (Cueto-Felgueroso & Juanes, 2009b). Thus, we find that not all snow property values produce saturation overshoot.

### 4.3 Non-isothermal preferential infiltration

We now consider the full model in 2D and investigate the non-isothermal problem of melt at  $0^\circ\text{C}$  infiltrating into an initially subfreezing snowpack of  $T = -10^\circ\text{C}$ . We adopt the same snow properties and simulation setup as Section 4.2 and take  $\text{SSA}_0 = 3514 \text{ m}^{-1}$  (see also Section 4.1.3). The only difference with respect to Section 4.2 is the initial ice temperature ( $T_{i,0}$ ) and the ice temperature on the bottom boundary ( $T_{i,\text{bot}}$ ). Here we impose an uniform ice temperature initially:  $T_{i,0} = T_{i,\text{bot}} = -10^\circ\text{C}$ . The initial  $T_i$  distribution is discontinuous at the top boundary where  $T_{i,\text{top}} = T_{\text{melt}} = 0^\circ\text{C}$  (Section 3.1.1). Temperature profile of a real snowpack would exhibit a thermal gradient caused by surface heating or cooling. Thus, here the assumption of an initially uniform  $T_i$  is a simplification. As we show below, such simplification in initial  $T_i$  only affects the porosity evolution near the snow surface, as a thermal equilibrium quickly establishes beneath the surface and does not affect the infiltration and refreezing process



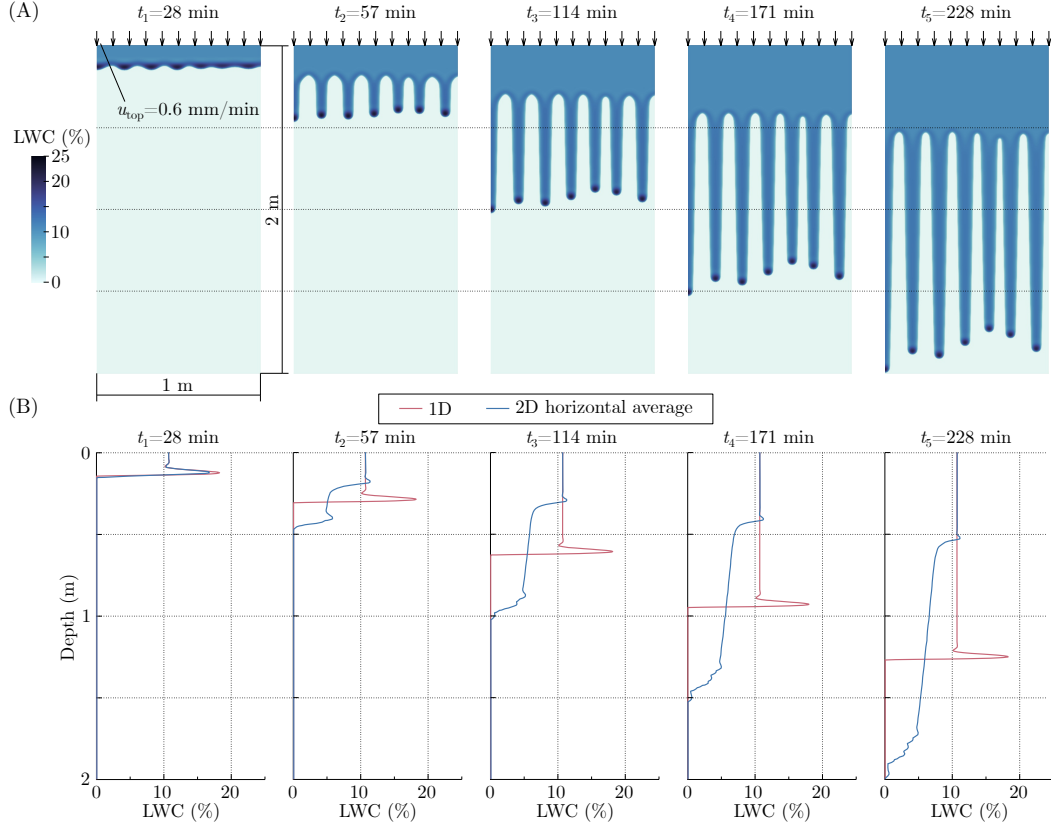


**Figure 7. Isothermal preferential infiltration through homogeneous snow.** LWC distribution at  $t = 28, 57, 114, 171$ , and  $228$  min. (A) 2D simulation results. (B) 1D (red line, stable flow) and horizontally averaged 2D (blue line, unstable flow) simulation results. The 1D and 2D simulations are performed with the same initial conditions and parameter values. We consider a constant influx rate  $u_{top}$ . See Video S1 in the Supporting Information.

underneath. As done in the previous section, we also run an equivalent 1D simulation to compare stable (1D) and unstable (2D) infiltration.

We show the simulation results at four different times in Fig. 8. The left-hand side of the figure displays the LWC, porosity,  $T_i$ , and  $T_w$  distributions (from top to bottom) of the 2D simulation. The right-hand side of Fig. 8 shows the LWC, porosity,  $T_i$ , and  $T_w$  profiles (from top to bottom) of the 1D simulation (red line) and the corresponding horizontally averaged distributions of the 2D simulation (blue line).

At the initial times ( $t \approx 57$  min) the LWC displays an initial set of fingers which are vertical and roughly uniformly spaced, similarly to the isothermal case (see Fig. 7A). The refreezing of melt leads to porosity decrease in melt-occupied region (Fig. 8B, left).

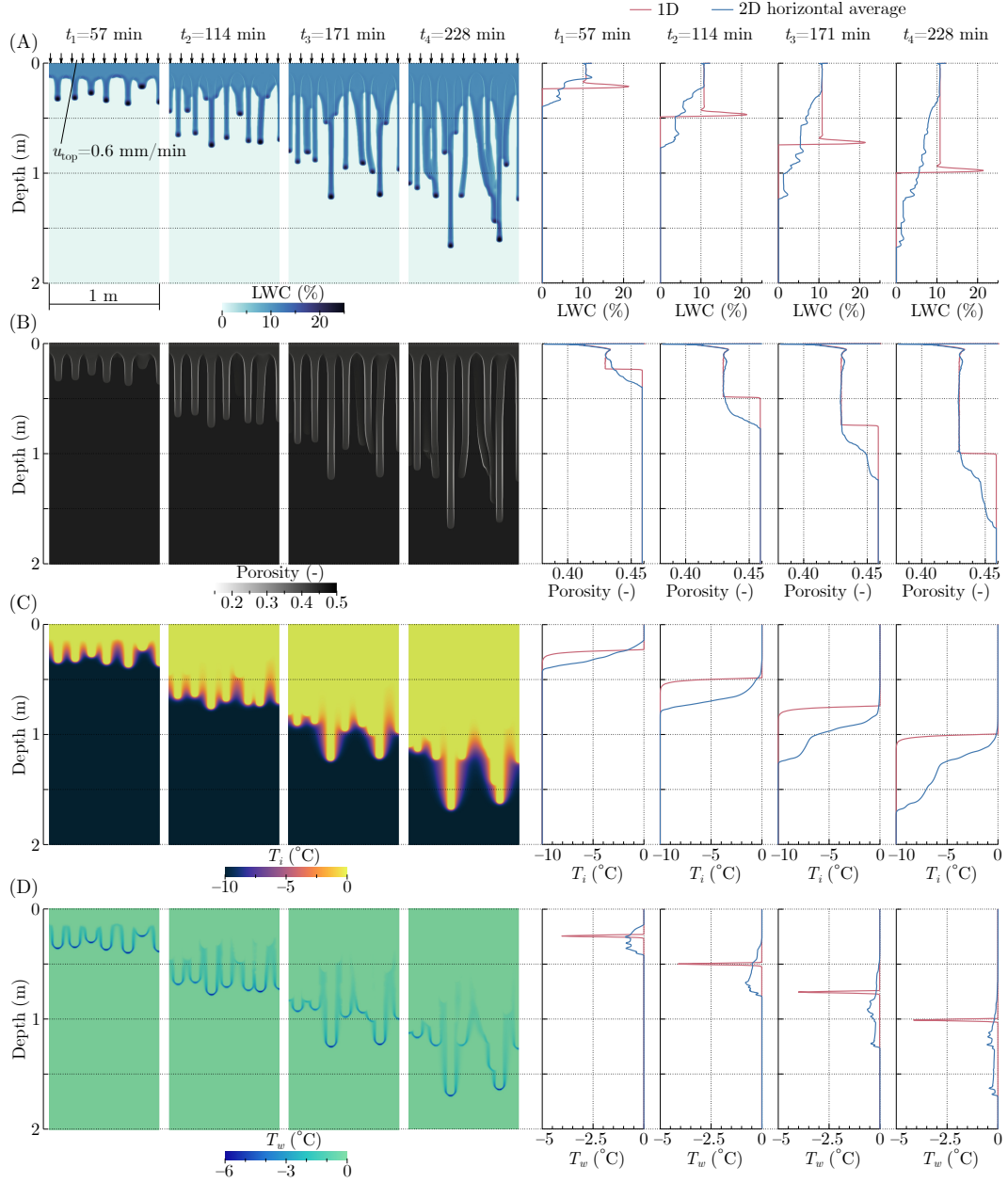


**Figure 8. Non-isothermal preferential infiltration through homogeneous snow.** (A) LWC, (B) porosity, (C)  $T_i$ , and (D)  $T_w$  distributions at  $t = 57, 114, 171$ , and  $228$  min. Left: 2D simulation snapshots. Right: 1D (red line, stable flow) and horizontally-averaged 2D (blue line, unstable flow) simulation results. See video S2 in the Supporting Information.

The porosity distributions at  $t = 57$  and  $114$  min show the onset of ice piping, i.e., the formation of a low porosity annulus surrounding the fingers, which may correspond to the ice pipes observed in Humphrey et al. (2012). Within each melt finger, ice temperature quickly reaches  $T_{\text{melt}} = 0^\circ\text{C}$  due to rapid heat exchange with the melt phase. Therefore, melt within the fingers does not freeze completely and the finger interior remains porous. Along the finger interface, however, melt can continue to refreeze due to the diffusion of cold content from the surrounding un-infiltrated snow. Overall, this results in significantly more porosity decrease along the finger interface than finger interior, leading to the formation of ice pipes (Fig. 8B, left).

Our results thus far show that melt refreezing dynamically changes the porosity structure of the initially homogeneous snowpack, leading to highly heterogeneous permeability fields. Such structural change significantly impacts ensuing melt transport and produces flow behaviors that are drastically different from isothermal infiltration (Section 4.2). For instance, at  $t = 114$  min, the LWC displays a set of secondary fingers, different from the initial ones, which emerge in regions of higher porosity in between the initial fingers (Fig. 8A, left). These secondary fingers seek regions of higher porosity, forming meandering paths that are initially independent but eventually merge with pre-existing melt channels ( $t = 228$  min in Fig. 8A, left). Note that the width of fingers, which indicate melt-occupation, becomes thinner as the ice pipe structures grow and consumes melt locally ( $t = 57$  and  $114$  min in Fig. 8A, left). The arrival of the first set of fingers significantly warms the ice temperature due to heat exchange and the release of latent heat. Thus, we observe significantly weaker porosity reduction in these regions during the infiltration of secondary fingers. In addition, we also observe that the  $T_w$  distribution displays a region of supercooled water surrounding the fingering front (Fig. 8D, left, also see Section 4.1.3).

The right-hand side of Fig. 8 shows the difference between stable (1D, red line) and unstable (2D, blue line) meltwater flow. As observed in isothermal infiltration, unstable flow reaches deeper points faster than stable flow (Fig. 8A, right). For that reason, changes in porosity and  $T_i$  are observed deeper in the snowpack for unstable infiltration (Figs. 8B and 8C, left). The discontinuity in porosity profile at the snow surface is caused by the discontinuity in the imposed initial  $T_i$ . However, such discontinuity does not affect the infiltration and refreezing process deeper in the snowpack. While the rate of melt arrival at the top of the snowpack is the same in both 1D and 2D simulations, we find

that the total change in porosity and in  $T_i$  is larger for unstable infiltration (2D). These results show that unstable infiltration enhances the refreezing process by creating more melt/ice interfaces that promote thermal exchange and melt refreezing.

In addition, Fig. 8B, left shows another interesting result: the change in porosity above the stable (1D) wetting front is the same for the horizontally-averaged 2D results, despite the highly nonlinear nature of the 2D problem. Moreover, if we disregard the discontinuity at the snow surface, the porosity distribution is approximately uniform in points above the stable wetting front. This behavior differs from the results in Section 4.1.3, in which the porosity displays a non-uniform distribution (e.g., day 203 in Fig. 5B). As we mentioned in Section 4.1.3, the infiltration and refreezing process depends on the interplay between the meltwater flow velocity, the advective and diffusive heat transport rates, and the ice-water phase change rate. In this section, we consider a meltwater influx rate ( $u_{\text{top}}$ ) larger than in Section 4.1.3, which could explain the differences observed in the porosity profiles during refreezing events.

## 5 Discussion

### 5.1 The influence of preferential infiltration on melt transport

We have shown that preferential infiltration delivers melt faster to deeper depth compared to stable infiltration (Fig. 7B), as is expected for unstable infiltration in typical porous media (DiCarlo, 2013). In the context of melt refreezing during transport, our results show that preferential infiltration facilitates more melt to reach deeper parts of the snow before becoming frozen (see Fig. 8A, right). As a consequence, changes in ice temperature and porosity occurs in deeper parts of the snow under preferential infiltration (Figs. 8B-C, right). To this end, our work joins previous efforts (Hirashima et al., 2019; Leroux et al., 2020) to show that preferential flow has a strong impact in the fate of meltwater transport in snow and, in particular, prolongs the travel paths of melt.

### 5.2 The influence of refreezing on melt infiltration

Melt refreezing directly impacts infiltration by reducing the amount of meltwater available for transport. In Fig. 9, we compare the results from isothermal and non-isothermal preferential infiltration shown in Figs. 7 and 8 by plotting the 2D LWC distribution (Fig. 9A) and the horizontally-averaged LWC profile (Fig. 9B) at five different times. The direct

comparison shows that, indeed, isothermal infiltration reaches deeper depth than infiltration under refreezing, and the total amount of water that remains as the melt phase (depth-integration of the curves in Fig. 9B) is less due to refreezing. The reduced infiltration depth is also caused, to a lesser extent, by a porosity decrease in the initial fingers which promotes the formation of secondary fingers in new locations and thus diverts flow away from the pre-established melt channels (Figs. 8A-B, left).

The 2D results shown in this paper assume an initially homogeneous snow to allow us to focus on heterogeneous melt flow due to gravity-driven flow instability. In practice, snowpack porosity structure is highly heterogeneous, as it is dynamically shaped by intermittent snowfalls, snow compaction, and snow metamorphism (Armstrong & Brun, 2008; Rempel, 2007; Jones & Orville-Thomas, 2012). Here, we demonstrate that melt refreezing is another important mechanism that reshapes the porosity structure of the snowpack and could significantly influence melt transport (Culberg et al., 2021). Compared to isothermal infiltration, we show that the interaction between an evolving porosity structure and channelized flow exacerbates the nonlinear nature of the flow (Fig. 9A). The subject of how pre-existing porosity structures (e.g. layers and lenses) impact melt transport will be the focus in future studies.

### 5.3 Improvements and extensions of the model

In comparison to existing models which often assume equilibrium thermodynamics or impose empirical estimations of phase change kinetics, a key feature of the model presented here is a physically-resolved treatment of the ice-water phase change kinetics at the continuum scale. Our approach results from upscaling the Wilson-Frenkel law that relates the ice growth rate and the temperature at the ice-water interface. To estimate the interface temperature at the Darcy scale ( $T_{\text{int}}$ ), we leverage the Gibbs-Thomson condition and the thermal energy conservation at the ice-water interface. The estimated value of  $T_{\text{int}}$  depends only on two physical parameters,  $r_i$  and  $r_w$ , that represent characteristic thermal diffusion lengths and require calibration. Preliminary results show that the model results are robust to the assumptions of  $r_i$  and  $r_w$ , although further research is needed. The model can also be readily extended to account for the solar heat flux that induces melting in the upper layers of the snowpack. Although we do not investigate melting in this work, it will be explored in future works.

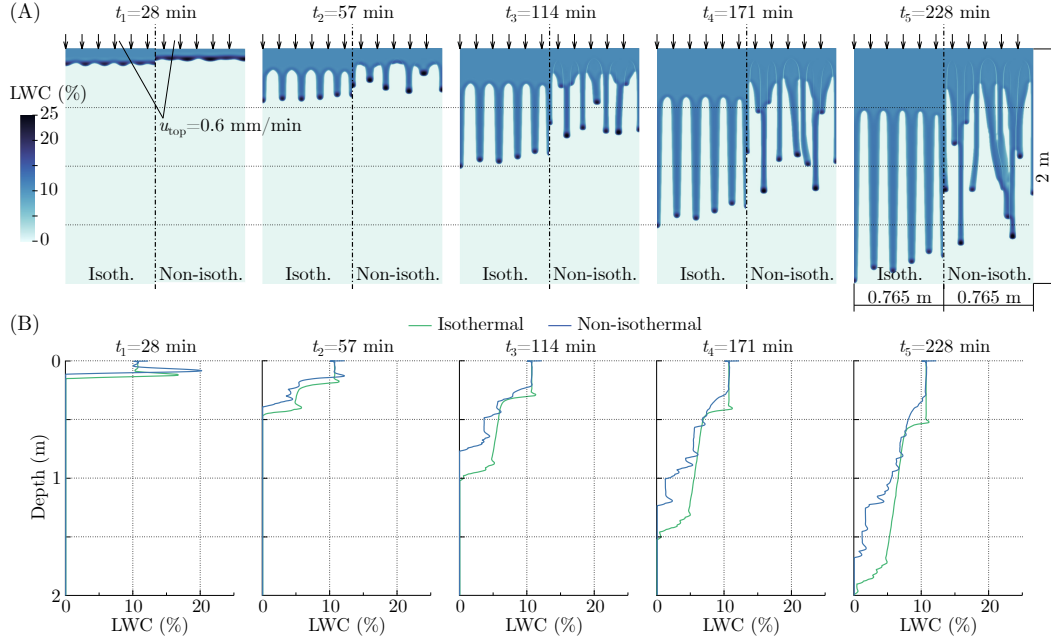


**Figure 9. Comparison between isothermal and non-isothermal unstable infiltration.** (A) LWC at  $t = 28, 57, 114, 171,$  and  $228$  min for isothermal (left half) and non-isothermal (right half) infiltration. (B) Horizontally-averaged LWC at  $t = 28, 57, 114, 171,$  and  $228$  min for isothermal (green) and non-isothermal (blue) infiltration. The results correspond to the simulations shown in Figs. 7 and 8.

#### 5.4 A need for well-controlled experiments of melt infiltration

We present a Darcy-scale model that accounts for preferential meltwater infiltration and refreezing through snow. Previous models of unstable melt infiltration (Hirashima et al., 2014; Leroux & Pomeroy, 2017; Leroux et al., 2020) build upon the Richards equation and require heterogeneous snow properties combined with imbibition/draining hysteresis and/or dynamic capillary pressure to capture flow instability. In comparison, our model incorporates a Richards-like equation extended with a higher-order term in saturation (Eq. (7)) that robustly reproduces the formation of preferential flow in homogeneous snow with a small number of parameters (Fig. 7). The reduced complexity of this model allows us to directly compare against existing experiments at the centimeter scale as well as field data at the meter scale. The comparison with limited laboratory experiments (Sec.4.1.1 and 4.1.2) have shown that the model can reproduce the temporal dynamics of capillary pressure and the rate of infiltration with reasonable accu-

racy. However, our results generally underestimates the magnitude of capillary pressure overshoot in snow (see Fig. 4), which could be amended by imposing an imbibition/drainage hysteresis in the capillary pressure (Leroux et al., 2020). At the larger scale, we have compared against field measurements of temperature profiles in Sec. 4.1.3 and find good agreement with minimal parameter tuning. However, it is challenging to validate/verify other aspects of this model due to the lack of more detailed experimental observations. For instance, we are not able to directly compare the patterns of infiltration (e.g. width of fingers) against experiments, although we did find that, in order to capture cm-wide fingers observed in Avanzi et al. (2016),  $h_{\text{cap}}$  and the exponent  $a$  in relative permeability need to be tuned (see Remark in Sec. 4.1.2). On the other hand, there has only be limited field evidence that supports the emergence of low-porosity structures predicted in this model (Sec.4.3), and a systematic investigation of its formation process in the laboratory is lacking. The development of well-controlled experiments will be a focus on our future work, and will allow us to further understand the mechanisms behind unstable infiltration in snow.

## 6 Conclusions

We present a model that resolves the nonlinear coupling of preferential melt flow and the nonequilibrium thermodynamics of ice-melt phase change to investigate the influence of melt refreezing in the overall efficiency of melt transport. We validate the model in 1D against laboratory infiltration experiments in snow and find good agreement in the point-wise pressure profile and its temporal dynamics. Comparison against 1D temperature profiles measured along a 10m-deep snow section in Greenland demonstrates that our model captures the thermal signatures of melt infiltration and refreezing at the meter-scale. We then use our model to study the differences between stable and unstable infiltration under isothermal and non-isothermal scenarios in 2D. The results demonstrate that, compared to stable infiltration, unstable infiltration delivers melt to deeper parts of the snowpack and prolongs the travel paths of melt. Thus, changes in porosity and the thermal profile incur at deeper depths due to preferential infiltration. When melt infiltrates into subfreezing snow, our model demonstrates that melt refreezing is an important mechanism that actively reshapes the porosity structure of the snow. In particular, our model readily captures the formation of ice pipes that have been observed in the field. The dynamic coupling between preferential infiltration and melt refreezing re-

sults in highly meandering melt pathways. However, we find that, melt and ice phase can quickly establish a thermal equilibrium ( $T = 0^\circ\text{C}$ ) upon the arrival of the first set of melt fingers, allowing ensuing melt to bypass this region without refreezing. Such mechanism may help deliver melt over long distances without refreezing and might play an important role in snow avalanches, perennial firn aquifers, and snow melt breakthrough events.

In this work, we focus on exploring the model results under one specific set of environmental parameter values (e.g.  $T_i$ ,  $u_{\text{top}}$ ,  $\phi_0$ ). In future work, the model can be readily used to gain insight into the role of pre-existing porosity/permeability heterogeneity in snowpack and the role of temporal variability of surface conditions during diurnal or seasonal cycles. The model may help improve the mechanistic understanding of how melt transports in snow under dynamic environmental conditions and advance the predictive capability in hydrology to understand how Earth’s largest freshwater resource will respond to climate change.

## Acknowledgments

XF, AM and NJ acknowledge the support of the Resnick Sustainability Institute at California Institute of Technology. CM acknowledges support from the Heising-Simons Foundation (# 2020-1911) and the William H. Neukom Institute for Computational Science at Dartmouth College. JP acknowledges the support of the Caltech Summer Undergraduate Research Fellowship. The authors also acknowledge the insightful discussions with David DiCarlo, Marc Hesse, Dani Or, John Selker, Riley Culberg, Quirine Krol, Ian Hewitt, and Nicolas Leroux.

AM, CM, and XF designed the study. AM and XF developed the model. AM implemented the model numerically and performed numerical simulations. NJ and JP helped with model validation against experimental data. AM, NJ, JP, CM, and XF analyzed the results and wrote the paper. XF secured funding for this project.

## Data Availability Statement

Datasets for this research are available in Moure et al. (2022), and can be directly accessed at <https://data.caltech.edu/records/vyfm3-jjk97>.



## References

- Armstrong, R. L., & Brun, E. (2008). *Snow and climate: physical processes, surface energy exchange and modeling*. Cambridge University Press.
- Aschwanden, A., Bueler, E., Khroulev, C., & Blatter, H. (2012). An enthalpy formulation for glaciers and ice sheets. *Journal of Glaciology*, 58(209), 441–457.
- Avanzi, F., Hirashima, H., Yamaguchi, S., Katsushima, T., & Michele, C. D. (2016). Observations of capillary barriers and preferential flow in layered snow during cold laboratory experiments. *The Cryosphere*, 10(5), 2013–2026.
- Balay, S., Abhyankar, S., Adams, M. F., Benson, S., Brown, J., Brune, P., ... Zhang, J. (2022). *PETSc Web page*. <https://petsc.org/>. Retrieved from <https://petsc.org/>
- Bear, J. (1972). Dynamics of fluids in porous media. elsevier, new york. *Dynamics of fluids in porous media. Elsevier, New York.*
- Beljadid, A., Cueto-Felgueroso, L., & Juanes, R. (2020). A continuum model of unstable infiltration in porous media endowed with an entropy function. *Advances in Water Resources*, 144, 103684.
- Brooks, R. H., & Corey, A. T. (1966). Properties of porous media affecting fluid flow. *Journal of the irrigation and drainage division*, 92(2), 61–88.
- Calonne, N., Geindreau, C., Flin, F., Morin, S., Lesaffre, B., Rolland du Roscoat, S., & Charrier, P. (2012). 3-d image-based numerical computations of snow permeability: links to specific surface area, density, and microstructural anisotropy. *The Cryosphere*, 6(5), 939–951.
- Campbell, F. M., Nienow, P. W., & Purves, R. S. (2006). Role of the supraglacial snowpack in mediating meltwater delivery to the glacier system as inferred from dye tracer investigations. *Hydrological Processes: An International Journal*, 20(4), 969–985.
- Chung, J., & Hulbert, G. (1993). A time integration algorithm for structural dynamics with improved numerical dissipation: the generalized- $\alpha$  method.
- Clerx, N., Machguth, H., Tedstone, A., Jullien, N., Wever, N., Weingartner, R., & Roessler, O. (2022). In situ measurements of meltwater flow through snow and firn in the accumulation zone of the sw greenland ice sheet. *EGUsphere*, 1–31.
- Colbeck, S. (1972). A theory of water percolation in snow. *Journal of glaciology*,

- 679       11(63), 369–385.
- 680       Colbeck, S. C. (1976). An analysis of water flow in dry snow. *Water Resources Re-*  
681       *search*, 12(3), 523–527.
- 682       Cueto-Felgueroso, L., & Juanes, R. (2008). Nonlocal interface dynamics and pattern  
683       formation in gravity-driven unsaturated flow through porous media. *Physical Re-*  
684       *view Letters*, 101(24), 244504.
- 685       Cueto-Felgueroso, L., & Juanes, R. (2009a). Adaptive rational spectral methods for  
686       the linear stability analysis of nonlinear fourth-order problems. *Journal of Compu-*  
687       *tational Physics*, 228(17), 6536–6552.
- 688       Cueto-Felgueroso, L., & Juanes, R. (2009b). A phase field model of unsaturated  
689       flow. *Water resources research*, 45(10).
- 690       Cueto-Felgueroso, L., Suarez-Navarro, M. J., Fu, X., & Juanes, R. (2020a). Interplay  
691       between fingering instabilities and initial soil moisture in solute transport through  
692       the vadose zone. *Water*, 12(3), 917.
- 693       Cueto-Felgueroso, L., Suarez-Navarro, M. J., Fu, X., & Juanes, R. (2020b). Nu-  
694       merical simulation of unstable preferential flow during water infiltration into  
695       heterogeneous dry soil. *Water*, 12(3), 909.
- 696       Culberg, R., Schroeder, D. M., & Chu, W. (2021). Extreme melt season ice layers  
697       reduce firn permeability across greenland. *Nature communications*, 12(1), 1–9.
- 698       Dalcin, L., Collier, N., Vignal, P., Côrtes, A., & Calo, V. (2016). Petiga: A frame-  
699       work for high-performance isogeometric analysis. *Computer Methods in Ap-*  
700       *plied Mechanics and Engineering*, 308, 151–181. doi: [https://doi.org/10.1016/](https://doi.org/10.1016/j.cma.2016.05.011)  
701       j.cma.2016.05.011
- 702       De Michele, C., Avanzi, F., Ghezzi, A., & Jommi, C. (2013). Investigating the dy-  
703       namics of bulk snow density in dry and wet conditions using a one-dimensional  
704       model. *The Cryosphere*, 7(2), 433–444.
- 705       DiCarlo, D. A. (2004). Experimental measurements of saturation overshoot on infil-  
706       tration. *Water Resources Research*, 40(4).
- 707       DiCarlo, D. A. (2010). Can continuum extensions to multiphase flow models de-  
708       scribe preferential flow? *Vadose Zone Journal*, 9(2), 268–277.
- 709       DiCarlo, D. A. (2013). Stability of gravity-driven multiphase flow in porous media:  
710       40 years of advancements. *Water Resources Research*, 49(8), 4531–4544.
- 711       Domine, F., Taillandier, A.-S., & Simpson, W. R. (2007). A parameterization of

- the specific surface area of seasonal snow for field use and for models of snowpack evolution. *Journal of Geophysical Research: Earth Surface*, 112(F2).
- Eliassi, M., & Glass, R. J. (2003). On the porous continuum-scale modeling of gravity-driven fingers in unsaturated materials: Numerical solution of a hypodiffusive governing equation that incorporates a hold-back-pile-up effect. *Water resources research*, 39(6).
- Frenkel, J., & Joffe, A. (1932). On the electric and photoelectric properties of contacts between a metal and a semiconductor. *Physical Review*, 39(3), 530.
- Geiger, S. L., & Durnford, D. S. (2000). Infiltration in homogeneous sands and a mechanistic model of unstable flow. *Soil Science Society of America Journal*, 64(2), 460–469.
- Glass, R., & Nicholl, M. (1996). Physics of gravity fingering of immiscible fluids within porous media: An overview of current understanding and selected complicating factors. *Geoderma*, 70(2-4), 133–163.
- Glass, R., Steenhuis, T., & Parlange, J.-Y. (1989). Wetting front instability: 2. experimental determination of relationships between system parameters and two-dimensional unstable flow field behavior in initially dry porous media. *Water Resources Research*, 25(6), 1195–1207.
- Gomez, H., Bures, M., & Moure, A. (2019). A review on computational modelling of phase-transition problems. *Philosophical Transactions of the Royal Society A*, 377(2143), 20180203.
- Gomez, H., Cueto-Felgueroso, L., & Juanes, R. (2013). Three-dimensional simulation of unstable gravity-driven infiltration of water into a porous medium. *Journal of Computational Physics*, 238, 217–239.
- Hamidi, S., Heinze, T., Galvan, B., & Miller, S. (2019). Critical review of the local thermal equilibrium assumption in heterogeneous porous media: Dependence on permeability and porosity contrasts. *Applied Thermal Engineering*, 147, 962–971.
- Hansen-Goos, H., & Wettlaufer, J. (2010). Theory of ice premelting in porous media. *Physical Review E*, 81(3), 031604.
- Heinze, T. (2021). A multi-phase heat transfer model for water infiltration into frozen soil. *Water Resources Research*, 57(10), e2021WR030067.
- Hirashima, H., Avanzi, F., & Wever, N. (2019). Wet-snow metamorphism drives the transition from preferential to matrix flow in snow. *Geophysical Research Letters*,

- 745 46(24), 14548–14557.
- 746 Hirashima, H., Avanzi, F., & Yamaguchi, S. (2017). Liquid water infiltration into  
 747 a layered snowpack: evaluation of a 3-d water transport model with laboratory  
 748 experiments. *Hydrology and Earth System Sciences*, 21(11), 5503–5515.
- 749 Hirashima, H., Yamaguchi, S., & Katsushima, T. (2014). A multi-dimensional water  
 750 transport model to reproduce preferential flow in the snowpack. *Cold Regions Sci-*  
 751 *ence and Technology*, 108, 80–90.
- 752 Hughes, T. J., Cottrell, J. A., & Bazilevs, Y. (2005). Isogeometric analysis: Cad, fi-  
 753 nite elements, nurbs, exact geometry and mesh refinement. *Computer methods in*  
 754 *applied mechanics and engineering*, 194(39-41), 4135–4195.
- 755 Humphrey, N. F., Harper, J. T., & Pfeffer, W. T. (2012). Thermal tracking of  
 756 meltwater retention in greenland’s accumulation area. *Journal of Geophysical*  
 757 *Research: Earth Surface*, 117(F1).
- 758 Illangasekare, T. H., Walter Jr, R. J., Meier, M. F., & Pfeffer, W. T. (1990). Mod-  
 759 eling of meltwater infiltration in subfreezing snow. *Water Resources Research*,  
 760 26(5), 1001–1012.
- 761 Jansen, K. E., Whiting, C. H., & Hulbert, G. M. (2000). A generalized- $\alpha$  method  
 762 for integrating the filtered navier–stokes equations with a stabilized finite element  
 763 method. *Computer methods in applied mechanics and engineering*, 190(3-4),  
 764 305–319.
- 765 Jones, H. G., & Orville-Thomas, W. J. (2012). *Seasonal snowcovers: physics, chem-*  
 766 *istry, hydrology* (Vol. 211). Springer Science & Business Media.
- 767 Kaempfer, T. U., & Schneebeli, M. (2007). Observation of isothermal metamorphism  
 768 of new snow and interpretation as a sintering process. *Journal of Geophysical Re-*  
 769 *search: Atmospheres*, 112(D24).
- 770 Karma, A., & Rappel, W.-J. (1996). Phase-field method for computationally effi-  
 771 cient modeling of solidification with arbitrary interface kinetics. *Physical review E*,  
 772 53(4), R3017.
- 773 Karma, A., & Rappel, W.-J. (1998). Quantitative phase-field modeling of dendritic  
 774 growth in two and three dimensions. *Physical review E*, 57(4), 4323.
- 775 Katsushima, T., Yamaguchi, S., Kumakura, T., & Sato, A. (2013). Experimental  
 776 analysis of preferential flow in dry snowpack. *Cold Regions Science and Technol-*  
 777 *ogy*, 85, 206–216.

- 778 Kinar, N., & Pomeroy, J. (2015). Measurement of the physical properties of the  
779 snowpack. *Reviews of Geophysics*, 53(2), 481–544.
- 780 Koponen, A., Kataja, M., & Timonen, J. (1997). Permeability and effective porosity  
781 of porous media. *Physical Review E*, 56(3), 3319.
- 782 Lazzaro, A., Wismer, A., Schneebeli, M., Erny, I., & Zeyer, J. (2015). Microbial  
783 abundance and community structure in a melting alpine snowpack. *Extremophiles*,  
784 19(3), 631–642.
- 785 Leroux, N. R., Marsh, C. B., & Pomeroy, J. W. (2020). Simulation of preferential  
786 flow in snow with a 2-d non-equilibrium richards model and evaluation against  
787 laboratory data. *Water Resources Research*, 56(9), e2020WR027466.
- 788 Leroux, N. R., & Pomeroy, J. W. (2017). Modelling capillary hysteresis effects on  
789 preferential flow through melting and cold layered snowpacks. *Advances in Water  
790 Resources*, 107, 250–264.
- 791 Leroux, N. R., & Pomeroy, J. W. (2019). Simulation of capillary pressure overshoot  
792 in snow combining trapping of the wetting phase with a nonequilibrium richards  
793 equation model. *Water Resources Research*, 55(1), 236–248.
- 794 Libbrecht, K. G. (2017). Physical dynamics of ice crystal growth. *Annual Review of  
795 Materials Research*, 47, 271–295.
- 796 Matzl, M., & Schneebeli, M. (2006). Measuring specific surface area of snow by near-  
797 infrared photography. *Journal of Glaciology*, 52(179), 558–564.
- 798 Meyer, C. R., & Hewitt, I. J. (2017). A continuum model for meltwater flow through  
799 compacting snow. *The Cryosphere*, 11(6), 2799–2813.
- 800 Moure, A., Jones, N., Pawlak, J., Meyer, C., & Fu, X. (2022, Nov). *Available data  
801 of thermodynamic nonequilibrium model for preferential infiltration and refreezing  
802 of melt in snow*. CaltechDATA. Retrieved from [https://data.caltech.edu/  
803 records/vyfm3-jjk97](https://data.caltech.edu/records/vyfm3-jjk97)
- 804 Mualem, Y. (1976). A new model for predicting the hydraulic conductivity of unsat-  
805 urated porous media. *Water resources research*, 12(3), 513–522.
- 806 Rempel, A. (2007). Formation of ice lenses and frost heave. *Journal of Geophysical  
807 Research: Earth Surface*, 112(F2).
- 808 Selker, J., Steenhuis, T., & Parlange, J.-Y. (1992). Wetting front instability in ho-  
809 mogeneous sandy soils under continuous infiltration. *Soil Science Society of Amer-  
810 ica Journal*, 56(5), 1346–1350.

- 811 Slater, B., & Michaelides, A. (2019). Surface premelting of water ice. *Nature Re-*  
 812 *views Chemistry*, 3(3), 172–188.
- 813 Van Genuchten, M. T. (1980). A closed-form equation for predicting the hydraulic  
 814 conductivity of unsaturated soils. *Soil science society of America journal*, 44(5),  
 815 892–898.
- 816 Waldner, P. A., Schneebeli, M., Schultze-Zimmermann, U., & Flühler, H. (2004). Ef-  
 817 fect of snow structure on water flow and solute transport. *Hydrological processes*,  
 818 18(7), 1271–1290.
- 819 Wilson, H. W. (1900). Xx. on the velocity of solidification and viscosity of super-  
 820 cooled liquids. *The London, Edinburgh, and Dublin Philosophical Magazine and*  
 821 *Journal of Science*, 50(303), 238–250.
- 822 Yamaguchi, S., Katsushima, T., Sato, A., & Kumakura, T. (2010). Water reten-  
 823 tion curve of snow with different grain sizes. *Cold Regions Science and Technol-*  
 824 *ogy*, 64(2), 87–93.
- 825 Yamaguchi, S., Watanabe, K., Katsushima, T., Sato, A., & Kumakura, T. (2012).  
 826 Dependence of the water retention curve of snow on snow characteristics. *Annals*  
 827 *of Glaciology*, 53(61), 6–12.

## 828 Appendix

### 829 Isothermal meltwater infiltration: problem formulation

830 By isothermal infiltration we refer to the case in which  $T_{i,\text{bot}} = T_{i,0} = T_{\text{melt}}$  (see  
 831 Section 3.1.1), i.e., the initial ice temperature, the initial water temperature, and the tem-  
 832 perature of the melt influx are fixed at the melting point. In that case, from Eq. (20)  
 833 we have  $T_{\text{int}}(\mathbf{x}, 0) = T_{\text{melt}}$  and, hence,  $\frac{\partial \phi}{\partial t}(\mathbf{x}, 0) = 0$ ,  $\frac{\partial T_i}{\partial t}(\mathbf{x}, 0) = 0$ , and  $\frac{\partial T_w}{\partial t}(\mathbf{x}, 0) =$   
 834  $0$ . These conditions lead to  $\phi(\mathbf{x}, t) = \phi_0$ ,  $T_i(\mathbf{x}, t) = T_{\text{melt}}$ , and  $T_w(\mathbf{x}, t) = T_{\text{melt}}$  for all  
 835  $t$ , which implies that we can disregard the porosity, ice temperature, and water temper-  
 836 ature evolution equations (Eqs.(23), (26), and (27)) and the right-hand side term in Eq. (24).  
 837 In the isothermal examples shown in Section 4, we only solve equations (24) and (25),  
 838 where we neglect the right-hand side of Eq. (24).

### Upscaling of the phase-change term

There are different methods to derive the upscaled phase-change term in Eq. (1). Here we present a simple approach that leverages the Wilson-Frenkel law (Wilson, 1900; Frenkel & Joffe, 1932) for ice growth —equivalent to the Gibbs-Thomson equation neglecting curvature; see Eq. (14). We start with the definition of the Darcy-scale ice mass  $m_i$ , which is the volume-averaged mass of ice in a REV:

$$m_i = \rho_i(1 - \phi) = \rho_i \frac{\int_{\Omega_{\text{ice}}} dx^P}{\int_{\Omega_{\text{REV}}} dx^P}, \quad (31)$$

where  $\Omega_{\text{REV}}$  represents the REV, which is fixed,  $\Omega_{\text{ice}}$  represents the ice phase in the REV, and we assumed a constant ice density  $\rho_i$ . Next, we take the time derivative of the ice mass, which reads

$$\frac{\partial m_i}{\partial t} = \rho_i \frac{\frac{\partial}{\partial t} \int_{\Omega_{\text{ice}}} dx^P}{\int_{\Omega_{\text{REV}}} dx^P}. \quad (32)$$

We can rewrite the time derivative of the ice volume in the REV as

$$\frac{\partial}{\partial t} \int_{\Omega_{\text{ice}}} dx^P = \int_{\Gamma_{iw}} v_n da, \quad (33)$$

where  $v_n$  is the normal velocity of the ice-water interface  $\Gamma_{iw}$ . Here, we assume that changes in the ice phase are caused by melting and freezing only. Thus, we use the Gibbs-Thomson condition (see Eq. (14)) and substitute  $v_n$  into Eq. (33) such that

$$\frac{\partial}{\partial t} \int_{\Omega_{\text{ice}}} dx^P = \int_{\Gamma_{iw}} -\frac{c_{p,w}}{\beta_{\text{sol}} L_{\text{sol}}} (T_{\text{int}}^P - T_{\text{melt}}) da = -\frac{c_{p,w}}{\beta_{\text{sol}} L_{\text{sol}}} (T_{\text{int}} - T_{\text{melt}}) \int_{\Gamma_{iw}} da, \quad (34)$$

where we neglected the curvature term ( $d_0$ ) and assumed that  $\overline{T_{\text{int}}^P} = T_{\text{int}}$ ; see Eq. (18).

The time derivative of the ice mass in the REV can be written as

$$\frac{\partial m_i}{\partial t} = -\rho_i \frac{c_{p,w}}{\beta_{\text{sol}} L_{\text{sol}}} (T_{\text{int}} - T_{\text{melt}}) \frac{\int_{\Gamma_{iw}} da}{\int_{\Omega_{\text{REV}}} dx^P} = -\rho_i \frac{c_{p,w}}{\beta_{\text{sol}} L_{\text{sol}}} (T_{\text{int}} - T_{\text{melt}}) W_{\text{SSA}}, \quad (35)$$

where  $W_{\text{SSA}}$  is the wet SSA, i.e., the surface of the ice-water interface in the REV divided by the REV volume. The right-hand side in Eq. (35) is identical to the phase-change term in Eq. (1). We could also derive the upscaled phase-change term in Eq. (1) from the pore-scale model for solidification introduced below; see Eqs. (36) and (37).

### Estimation of $r_i$ and $r_w$

We use pore-scale simulations to calibrate the parameters  $r_i$  and  $r_w$  (see Section 2.2.1). We solve a phase-field model for water solidification (Karma & Rappel, 1996; Gomez et al., 2019). The model includes a phase-field variable  $\phi^P(\mathbf{x}^P, t)$  which captures the ice

and water phases ( $\phi^P = 1$  in the ice and  $\phi^P = 0$  in the water) and displays a smooth transition at the interface. The model also includes a single temperature variable  $T^P(\mathbf{x}^P, t)$  defined in the entire domain  $\Omega_{\text{REV}}$ , which accounts for the temperature in the ice and water phases. The model equations can be written as

$$\tau \frac{\partial \phi^P}{\partial t} = \varepsilon^2 \nabla^2 \phi^P - \phi^P(1 - \phi^P)(1 - 2\phi^P) - \lambda \phi^{P^2}(1 - \phi^P)^2 \frac{T^P - T_{\text{melt}}}{L_{\text{sol}}/c_{p,w}}, \quad (36)$$

$$\rho(\phi^P)c_p(\phi^P) \frac{\partial T^P}{\partial t} = \nabla \cdot [K(\phi^P) \nabla T^P] + \rho(\phi^P)L_{\text{sol}} \frac{\partial \phi^P}{\partial t}, \quad (37)$$

where  $\tau$  and  $\lambda$  are two parameters related to the parameters  $\beta_{\text{sol}}$  and  $d_0$  defined in the Gibbs-Thomson condition; see Eq. (14). The parameter  $\varepsilon$  represents the phase-field interface width and the functions  $\rho(\phi^P)$ ,  $c_p(\phi^P)$ , and  $K(\phi^P)$  account for density, specific heat capacity, and thermal conductivity, respectively, of the ice and water phases. These functions are defined as  $\rho(\phi^P) = \rho_i \phi^P + \rho_w(1 - \phi^P)$ . Equivalent expressions are used for  $c_p(\phi^P)$  and  $K(\phi^P)$ . Karma & Rappel (1996, 1998) showed that Eqs. (36) and (37) tend to the generalized Stefan problem as  $\varepsilon \rightarrow 0$ . The authors also derived the relation between the parameters  $\tau$ ,  $\lambda$ ,  $\beta_{\text{sol}}$ , and  $d_0$ , which can be expressed as

$$d_0 = a_1 \frac{\varepsilon}{\lambda}, \quad \beta_{\text{sol}} = a_1 \left( \frac{\tau}{\varepsilon \lambda} - a_2 \frac{\varepsilon}{D_*} \right), \quad (38)$$

where  $D_* = (D_i + D_w)/2$  represents thermal diffusivity (see Eqs. (26) and (27)),  $a_1 \approx 5$ , and  $a_2 \approx 0.1581$  (Karma & Rappel, 1998).  $\varepsilon$  is a modeling parameter that must be small enough to fulfill certain conditions related to the ice grain geometry, the solidification kinetics, and the spatial discretization of the problem (Karma & Rappel, 1996, 1998).

Here, we consider a periodic 1D domain  $\Omega_{\text{REV}}$  with an ice grain in the center of the domain. We run simulations with different domain size  $L_P$  and ice grain diameter  $d_i$ . We consider three scenarios:  $(L_P, d_i) = (0.465, 0.2)$ ,  $(1.11, 0.6)$ , and  $(2.77, 1.5)$ mm, which correspond to porosity of 0.57, 0.46, and 0.46, respectively. These are similar to the porosity and ice grain size of snow types listed in Table 2. We assume that the water is initially at the melting point. We consider two initial ice temperatures ( $-8$  and  $-4^\circ\text{C}$ ) and three different values for  $\beta_{\text{sol}}$  (80, 120, and  $800 \text{ s m}^{-1}$ ). We take  $\varepsilon = 0.2 \mu\text{m}$  and  $d_0 = 0.38 \text{ nm}$ . The rest of the parameter values are listed in Table 1. We employ the numerical method described in Section 3.2 to run the  $3 \times 2 \times 3$  simulations. We com-



pute the Darcy-scale unknowns as

$$T_i^*(t) = \frac{\int_{\Omega_{\text{REV}}} \phi^P T^P \, dx^P}{\int_{\Omega_{\text{REV}}} \phi^P \, dx^P}, \quad T_w^*(t) = \frac{\int_{\Omega_{\text{REV}}} (1 - \phi^P) T^P \, dx^P}{\int_{\Omega_{\text{REV}}} (1 - \phi^P) \, dx^P}, \quad T_{\text{int}}^*(t) = \frac{\int_{\Omega_{\text{REV}}} \phi^P (1 - \phi^P) T^P \, dx^P}{\int_{\Omega_{\text{REV}}} \phi^P (1 - \phi^P) \, dx^P}, \quad (39)$$

where we included the symbol  $\star$  to indicate that they are computed from pore-scale simulations. We stop the simulations when  $|T_{\text{int}}^*(t)| < 0.01 \, ^\circ\text{C}$ . For each simulation, we consider a discrete set of 40 times  $\{t_j\}$  equally distributed between the initial and final time of each simulation, in which we do not include the initial time. In Figs. 10A and 10B we plotted the phase-field  $\phi^P$  and temperature  $T^P$  profiles, respectively, for the simulation with  $d_i = 0.2 \, \text{mm}$ ,  $\beta_{\text{sol}} = 80 \, \text{s m}^{-1}$ , and initial ice temperature  $-8 \, ^\circ\text{C}$  at times  $t_0$  (initial time),  $t_{13}$ ,  $t_{26}$ , and  $t_{40}$ .

We can write Eq. (20) as  $T_{\text{int}} = mT_i + nT_w$ , likewise as  $T_{\text{int}}/T_w = mT_i/T_w + n$ , where we consider temperature in  $^\circ\text{C}$  ( $T_{\text{melt}} = 0 \, ^\circ\text{C}$ ) and the parameters  $m$  and  $n$  only depend on  $r_i$ ,  $r_w$ , and  $\beta_{\text{sol}}$ . We compute the discrete set of values  $\{(T_{\text{int}}/T_w)_j^*\}$  and  $\{(T_i/T_w)_j^*\}$ , such that  $(T_{\text{int}}/T_w)_j^* = T_{\text{int}}^*(t_j)/T_w^*(t_j)$  and  $(T_i/T_w)_j^* = T_i^*(t_j)/T_w^*(t_j)$ . We perform least squares analysis (linear regression) to estimate the values  $m$  and  $n$  for each simulation. In Fig. 10C, we plotted the pairs  $\{(T_i/T_w)_j^*, (T_{\text{int}}/T_w)_j^*\}$  for the simulation shown in Figs. 10A and 10B. The  $3 \times 2 \times 3$  simulations exhibit a linear trend for  $\{(T_i/T_w)_j^*, (T_{\text{int}}/T_w)_j^*\}$  as shown in Fig. 10C, with the value of  $n$  close to zero. For each pore-scale simulation, we can compute  $r_i$  and  $r_w$  from the values of  $m$ ,  $n$ , and  $\beta_{\text{sol}}$ . We plotted  $r_i$  and  $r_w$  in Figs. 10D and 10E, respectively, for each simulation. Four values of  $r_w$  take large positive or negative values because  $n \approx 0$ , which implies that the Darcy-scale  $T_{\text{int}}$  does not depend on  $T_w$ . Negative  $r_w$  values imply that the linear approximation assumption made in Eq (19) is not valid and, hence, the temperature profile would be different from the profile shown in Fig. 2. The results of  $r_i$  and  $r_w$  suggest that (i)  $r_i$  (and  $r_w$ ) does not depend on  $\beta_{\text{sol}}$  (see Figs. 10D and E), (ii)  $r_i$  is proportional to  $d_i$  (see the horizontal trend of  $r_i/d_i$  in Fig. 10F), and (iii)  $r_w$  and  $r_i$  are proportional (see the horizontal trend of  $r_w/r_i$  in Fig. 10G). A detailed calibration of parameters  $r_i$  and  $r_w$  is beyond the scope of this paper. Here, we simply assume that  $r_i$  is proportional to  $d_i$  and  $r_w$  is proportional to  $r_i$ . We take  $r_i = 0.06d_i$  and  $r_w = 1.35r_i$ . Despite not being the best fit, this choice of values represents a good approximation for intermediate ice grain size (the dashed lines in Figs. 10F and 10G).

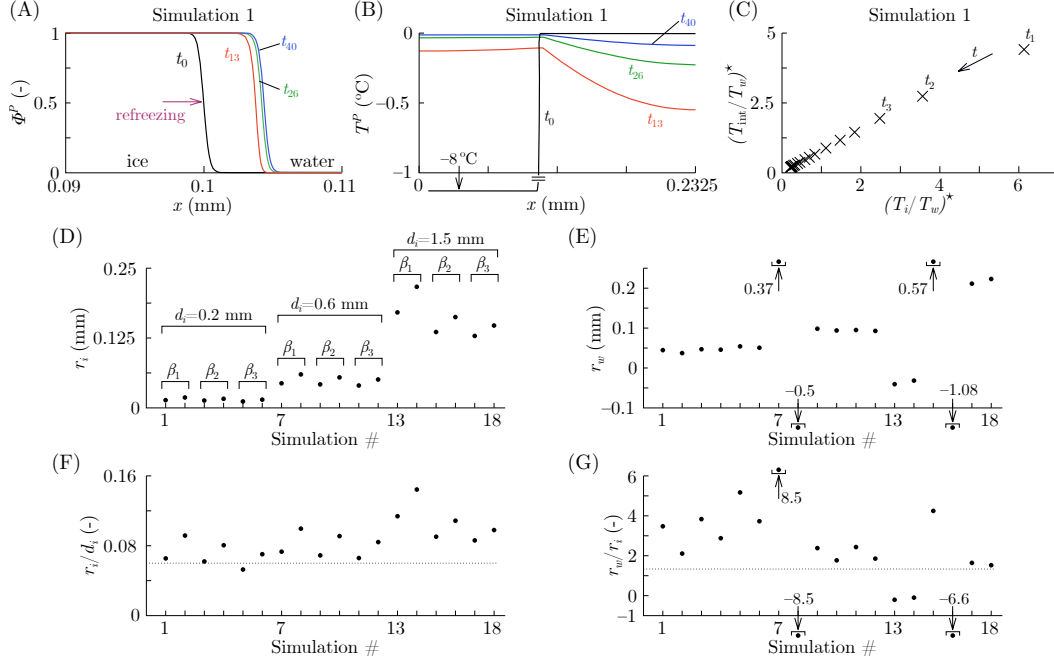


**Figure 10. Calibration of parameters  $r_i$  and  $r_w$ .** Time evolution of (A)  $\phi^P$  and (B)  $T^P$  for simulation 1 ( $d_i = 0.2$  mm,  $\beta_{\text{sol}} = 80$  s m $^{-1}$ , and initial ice temperature  $-8^\circ\text{C}$ ). The times  $t_j$  are defined in Appendix. (C) Pairs  $\{(T_i/T_w)_j^*, (T_{\text{int}}/T_w)_j^*\}$  of simulation 1. Values of (D)  $r_i$  and (E)  $r_w$  obtained from linear regression analysis for each simulation. The symbols  $\beta_1$ ,  $\beta_2$ , and  $\beta_3$  correspond to  $\beta_{\text{sol}} = 80$ , 200, and 800 s m $^{-1}$ , respectively. (F)  $r_i/d_i$  and (G)  $r_w/r_i$  for each simulation. Arrows in (E) and (G) indicate values that are outside the graphs range. The dashed lines in (F) and (G) represent the values we took to estimate  $r_i$  and  $r_w$  as a function of  $d_i$ .

**Remark:** We ran the non-isothermal simulations shown in Figs. 5 and 8 with different values of  $r_i$  and  $r_w$  ( $r_i = 0.41d_i$  and  $r_w = 2.4r_i$ ) and the results are very similar, which suggests that the influence of  $r_i$  and  $r_w$  is low. Further research is necessary to analyze the impact of  $r_i$  and  $r_w$  in our model.

### Regularity of functions $W_{\text{SSA}}$ , $k_r$ , $\psi$ , and $\kappa$

Our infiltration model displays minor  $S$  oscillations just downwards of the wetting front (Gomez et al., 2013). Thus,  $S$  may take negative values at some points in that area. To avoid singularities in the functions  $W_{\text{SSA}}$ ,  $k_r$ ,  $\psi$ , and  $\kappa$ , we need to define those functions for values  $S \leq 0$ . Our approach consists of setting a positive saturation value  $S_l$  close to zero (we took  $S_l = 10^{-3}$ ) and defining  $\mathcal{C}^0$ - or  $\mathcal{C}^1$ -continuous functions which

take the original value if  $S \geq S_l$  and a natural extension of those functions if  $S < S_l$ .

By natural extension we may refer to a value close to zero (e.g., in case of  $k_r$ ) or a function consistent with the flow potential (e.g., in case of  $\psi$ ).

We propose the following regularization for the functions  $W_{\text{SSA}}$ ,  $k_r$ ,  $\psi$ , and  $\kappa$ :

$$W_{\text{SSA}}(\phi, S) = \begin{cases} (S - S_l) \frac{\text{SSA}_0}{\phi_0 \ln(\phi_0)} \phi \ln(\phi) & \text{if } S \geq S_l, \\ 0 & \text{if } S < S_l. \end{cases} \quad (40)$$

$$k_r(S) = \begin{cases} S^a & \text{if } S \geq S_l, \\ S_l^a & \text{if } S < S_l, \end{cases} \quad (41)$$

$$\psi(S) = \begin{cases} h_{\text{cap}} S^{-\frac{1}{\alpha}} \left\{ 1 - \exp[\beta(S - \nu_e)] \left( 1 + \beta \frac{\alpha}{\alpha-1} S \right) \right\} & \text{if } S \geq S_l, \\ \psi_l + \psi'_l (S - S_l) & \text{if } S < S_l, \end{cases} \quad (42)$$

$$\kappa(S) = \begin{cases} h_{\text{cap}}^3 \frac{\alpha}{\alpha-1} S^{\frac{\alpha-1}{\alpha}} \{1 - \exp[\beta(S - \nu_e)]\} & \text{if } S \geq S_l, \\ 0.2\kappa_l + \frac{\kappa'_l}{2} \frac{(S - S_{\min})^2}{S_l - S_{\min}} & \text{if } S_{\min} \leq S < S_l, \\ 0.2\kappa_l & \text{if } S < S_{\min}, \end{cases} \quad (43)$$

where we substituted  $S_r = 0$  into the relative permeability ( $k_r$ ) function. In Eq. (42),  $\psi_l = \psi(S_l)$  and  $\psi'_l = \frac{d\psi}{dS}(S_l)$ . In Eq. (43),  $\kappa_l = \kappa(S_l)$ ,  $\kappa'_l = \frac{d\kappa}{dS}(S_l)$ , and  $S_{\min}$  is obtained from the equality  $\frac{\kappa'_l}{2}(S_l - S_{\min}) = 0.8\kappa_l$ . Eq. (40) implies that there is no phase change if  $S < S_l$ . Thus, the numerical parameter  $S_l$  may be interpreted as premelted water (or irreducible water saturation). According to Eq. (41), we numerically impose a tiny non-null relative permeability ( $S_l^a$ ) if  $S < S_l$ . If we consider  $k_r = 0$  for negative saturation values, the saturation may remain negative and infiltration may stop because  $\mathbf{u} = 0$ ; see Eq. (4). For the extension of the Leverett J-function  $\psi$ , we define a straight line which is tangent to the original  $\psi$  in  $S = S_l$ . According to this potential function, the saturation tends to increase (driven by the derivative of  $\psi$ ) if  $S < S_l$ . Finally, for  $\kappa$  we consider a quadratic convex function extension which is tangent to the original  $\kappa$  in  $S = S_l$ . The minimum value of the quadratic convex function is slightly higher than zero ( $0.2\kappa_l$ ) and is located in  $S = S_{\min}$ . For values  $S < S_{\min}$ , the function  $\kappa$  takes the constant value  $0.2\kappa_l$ .

The model equations are ill-posed in case  $\phi = 0$  or  $\phi = 1$ . We do not reach that situation in the simulations shown in this paper. The model can be readily adapted to account for the situation  $\phi = 0$  by numerically impose a minimum porosity slightly higher than zero and the situation  $\phi = 1$  by implementing an Arbitrary Lagrangian-Eulerian description. More details will be provided in future work.